Noname manuscript No.
(will be inserted by the editor)

Reynolds-averaged, scale-adaptive and large-eddy simulations of premixed bluff-body combustion using the Eddy Dissipation Concept

Dmitry A. Lysenko · Ivar S. Ertesvåg

Received: date / Accepted: date

Abstract A lean premixed propane/air bluff-body stabilized flame (Volvo test rig) is calculated using the Scale-Adaptive Simulation turbulence model (SAS) and Large-Eddy simulations (LES) as well as the conventional Reynolds-averaged approach (RAS). RAS and SAS are closed by the standard k-ϵ and the k-ω Shear Stress Transport (SST) turbulence models, respectively. The conventional Smagorinsky and the k-equation sub-grid scales models are used for the LES closure. Effects of the sub-grid scalar flux modeling using the classical gradient hypothesis and Clark's tensor diffusivity closures both for the inert and reactive LES flows are discussed. The Eddy Dissipation Concept (EDC) is used for the turbulence-chemistry interaction. It assumes that molecular mixing and the subsequent combustion occur in the 'fine structures' (smaller dissipative eddies, which are close to the Kolmogorov scales). Assuming the full turbulence energy cascade, the characteristic length and velocity scales of the 'fine structures' are evaluated using different turbulence models (RAS, SAS and LES). The finite-rate chemical kinetics is taken into account by treating the 'fine structures' as constant pressure and adiabatic homogeneous reactors, calculated as a system of ordinary-differential equations (ODEs) described by a Perfectly Stirred Reactor (PSR) concept. Several further enhancements to model the PSRs are proposed, including a new Livermore Solver (LSODA) for integrating stiff ODEs and a new correction to calculate the PSR time scales. All models have been implemented as a stand-alone application edcPisoFoam based on the OpenFOAM technology. Additionally, several RAS calculations

Dmitry A. Lysenko
3DM Simtek AS, Markveien 22, NO–4307, Sandnes, Norway
E-mail: dmitry.lysenko@edcpisofoam.com

Ivar S. Ertesvåg
Department of Energy and Process Engineering, NTNU Norwegian University of Science and Technology, Kolbjørn Hejes vei 1B, NO–7491, Trondheim, Norway
Tel.: +47-73-593755
Fax: +47-73-593580
E-mail: ivar.s.ertesvag@ntnu.no

were performed using the Turbulence Flame Speed Closure model in Ansys Fluent to assess effects of the heat losses by modeling the conjugate heat transfer between the bluff-body and the reactive flow. Effects of the turbulence Schmidt number on RAS results are discussed as well. Numerical results are compared with available experimental data. Reasonable consistency between experimental data and numerical results provided by RAS, SAS and LES is observed. In general, there is satisfactory agreement between present LES-EDC simulations, numerical results by other authors and measurements without any major modification to the EDC closure constants, which gives a quite reasonable indication on the adequacy and accuracy of the method and its further application for turbulent premixed combustion simulations.

Keywords · URANS · Eddy Dissipation Concept · Large Eddy Simulation · LSODA · Scale Adaptive Simulation · lean premixed bluff-body combustion · heat transfer · Volvo test rig · edcPisoFoam

1 Introduction

The long-term goal of the present work is to develop a large-eddy simulation model for high Reynolds number reactive and non-reactive flows of practical interest. The core numerical method is based on the OpenFOAM toolbox [67], which was originally developed as a high-end C++ classes library (Field Operation and Manipulation) for a broad range of fluid dynamics applications, but quickly became very popular in industrial engineering as well as in academic research.

Previously, methodical investigations for several plane turbulent bluff-body flows have been carried out with the goal of validation, verification and understanding of the capabilities of the numerical method using the conventional approach for solution of the steady/unsteady compressible Reynolds-averaged Navier-Stokes equations (RANS/URANS), which sometimes referred to as "Reynolds-averaged simulations" (RAS). These results were analyzed in detail and agreed fairly well with experimental data [31].

Recently, Lilleberg et al. [30] and Lysenko et al. [34], [35] carried out several turbulent combustion calculations of detailed flame experiments such as the Sandia Flames D,E [3], the piloted lean lean-premixed jet burner [14], [15], the Sandia Flame CHNa [4] and the Sydney Bluff-Body Flame HM1E [12]. These flames were calculated using the standard k-ϵ model [29]. The turbulence-chemistry interaction was treated via the Eddy Dissipation Concept (EDC) with the detailed chemistry [19] described by the full GRI-3.0 mechanism [6]. In general, there was good agreement between these simulations and measurements. It is believed that one of the main reasons for the observed discrepancies between the predictions and experimental data was the round-jet anomaly of the k-ϵ turbulence model. At the same time the EDC was extended for the large-eddy simulation and was validated against the Sandia Flame D [35]. Overall, these results [30], [34], [35] gave a good indication on

the adequacy and accuracy of the implemented solver and its readiness for further combustion application development.

In the present study, several enhancements of the framework have been introduced. First, the Scale-Adaptive Simulation (SAS) [44] has been implemented and integrated with the Eddy Dissipation Concept. Second, a new correction is proposed for the residence or mixing time scale (τ^*), which is used in the Perfectly Stirred Reactor concept. The conventional formulation for τ^* is based on the molecular viscosity and the dissipation rate [19],[16]. In the present study, τ^* additionally takes into account the influence of chemical time scales. Third, from the authors' previous experience [34], [35], the stiff ordinary-differential equations (ODEs, hereafter) integrator RADAU5 [20] failed with certain chemical kinetics schemes. Thus, a new ODEs integrator LSODA has been implemented to overcome this issue. LSODA is the Livermore solver [48], which includes a variable-step, variable-order Adams-Moulton method of orders 1 to 12 and a variable-step, variable-order backward differentiation formula method of orders 1 to 5.

Thus, the prime scope of this work was to provide further extension of the EDC validity for computation of turbulent premixed flames using the Large-Eddy simulations. Another goal was to provide validation of the implemented SAS model for the non-reactive flows and its further extension for the reactive flows coupled with the EDC.

The Volvo test rig has been chosen due to the available experimental data including high speed imaging, conventional gas analysis [58], Laser Dopler Anemometry (LDV) measurements of the velocity [59] and coherent anti-Stokes Raman scattering (CARS) measurements of the temperature [60]. Moreover, this case has been extensively used by other researchers to study turbulent premixed combustion (among of them [26], [36], [40], [51]).

Premixed turbulent combustion can be described as the interaction between a flame front, with thickness δ and speed S_L, and an ensemble of eddies representing turbulence. The eddies range in size from the Kolmogorov to the integral (l_t) length scale, and with characteristic speeds ranging from the Kolmogorov to the integral root-mean-squared (u') velocities. The present predictions showed that this flame was in the "thin reaction zone" regime [47].

The paper is divided into six main sections. The first and second sections of the paper describe the mathematical and numerical modeling, respectively. Then, a general description of the test cases is given. Finally, computational results are presented, results are analyzed and discussed, and conclusions are drawn.

2 Mathematical modeling

One of the possible approaches in modeling of turbulent reacting flows in the context of RANS/URANS is the Eddy Dissipation Concept (EDC). Initially developed in the 1970s [37], EDC was formulated as a well-established turbulent combustion closure model in the 1980s - 2000s [16], [19], [38].

In the present study a turbulent premixed bluff-body flame in the Volvo test rig was predicted by URANS, SAS and LES simulations coupled with the Eddy-Dissipation Concept. The same mathematical apparatus and numerical algorithm in the context of Reynolds-averaging and Large-Eddy simulations were applied as in the previous studies, respectively [34], [35]. Here, some new features of the method such as SAS-EDC are outlined.

Hereafter, the hat, the overbar and the tilde denote Favre-averaging, Reynolds-averaging and Favre-filtering, respectively.

2.1 Turbulence

– URANS: the Favre-averaged (i.e. mass-density-weighted), two-dimensional unsteady equations of mass, momentum and energy for turbulent flow were solved.
The standard k-ϵ model [29] is based on the turbulence kinetic energy ($\hat{k}$) and its dissipation rate ($\hat{\epsilon}$). The turbulence viscosity is defined here as $\mu_t = C_\mu \bar{\rho} \hat{k}^2 / \hat{\epsilon}$.
The modeled transport equations are:

$$\frac{\partial}{\partial t}\left(\bar{\rho}\hat{k}\right) + \frac{\partial}{\partial x_j}\left(\bar{\rho}\hat{k}\hat{\mathbf{u}}_j\right) = \frac{\partial}{\partial x_j}\left(\left(\mu + \frac{\mu_t}{\sigma_k}\right)\frac{\partial \hat{k}}{\partial x_j}\right) + G - \bar{\rho}\hat{\epsilon}, \qquad (1)$$

$$\frac{\partial}{\partial t}\left(\bar{\rho}\hat{\epsilon}\right) + \frac{\partial}{\partial x_j}\left(\bar{\rho}\hat{\epsilon}\hat{\mathbf{u}}_j\right) = \frac{\partial}{\partial x_j}\left(\left(\mu + \frac{\mu_t}{\sigma_\epsilon}\right)\frac{\partial \hat{\epsilon}}{\partial x_j}\right) + C_{\epsilon 1}\frac{\hat{\epsilon}}{\hat{k}}G - C_{\epsilon 2}\bar{\rho}\frac{\hat{\epsilon}^2}{\hat{k}}, \qquad (2)$$

where μ is the molecular viscosity, and the rate of turbulence kinetic energy production G is given as

$$G = -\mu_t \mathbf{S}^2, \qquad (3)$$

where $\mathbf{S}$ is the modulus of the mean rate-of-strain tensor. The standard values [29] were used for the model constants $C_\mu = 0.09$, $C_{\epsilon 1} = 1.44$, $C_{\epsilon 2} = 1.92$, $\sigma_k = 1$ and $\sigma_\epsilon = 1.3$. The further details of the implementation were provided in [34].

– SAS: the model was implemented strongly following Menter and Egorov [43] with a high wave number (HWN) damping [44] based on the Wall-Adapting Local Eddy-Viscosity (WALE) model [45]. The SAS model was based on the $k-\omega$ SST turbulence model [41] with updated coefficients from [42]. The full SAS model description was provided by Menter and Egorov [44], and a limited discussion of the model formulation is given here. Besides the Favre-averaged equations of mass, momentum and energy, two additional transport equations for the turbulence kinetic energy and the turbulence eddy frequency were solved:

$$\frac{\partial}{\partial t}\left(\bar{\rho}\hat{k}\right) + \frac{\partial}{\partial x_j}\left(\bar{\rho}\hat{k}\hat{\mathbf{u}}_j\right) = \frac{\partial}{\partial x_j}\left(\left(\mu + \frac{\mu_t}{\sigma_k}\right)\frac{\partial \hat{k}}{\partial x_j}\right) + G - \bar{\rho}c_\mu\hat{\omega}, \qquad (4)$$

$$\frac{\partial}{\partial t}\left(\bar{\rho}\hat{\omega}\right)+\frac{\partial}{\partial x_j}\left(\bar{\rho}\hat{\omega}\hat{\mathbf{u}}_j\right)=\frac{\partial}{\partial x_j}\left(\left(\mu+\frac{\mu_t}{\sigma_\omega}\right)\frac{\partial\hat{\omega}}{\partial x_j}\right)+\alpha\frac{\hat{\omega}}{\hat{k}}G-\bar{\rho}\beta\hat{\omega}^2+Q_{SAS}+\left(1-F_1\right)\frac{2\bar{\rho}}{\sigma_{\omega2}}\frac{1}{\hat{\omega}}\frac{\partial\hat{k}}{\partial x_j}\frac{\partial\hat{\omega}}{\partial x_j},\quad(5)$$

where

$$Q_{SAS}=\max\left[\bar{\rho}\zeta_2\kappa\mathbf{S}^2\left(\frac{L}{L_{vk}}\right)^2-C_{SAS}\frac{2\bar{\rho}\hat{k}}{\sigma_\phi}\max\left(\frac{1}{\hat{k}^2}\frac{\partial^2\hat{k}}{\partial x_j^2},\frac{1}{\hat{\omega}^2}\frac{\partial^2\hat{\omega}}{\partial x_j^2}\right),0\right].\quad(6)$$

The turbulence length scale, L, is defined as

$$L=\frac{\sqrt{\hat{k}}}{c_\mu^{1/4}\hat{\omega}},\quad(7)$$

and the von Kármán length scale, L_{vk}, is computed according to

$$L_{vk}=\max\left[\frac{\kappa\mathbf{S}}{\left|\frac{\partial^2}{\partial x_j^2}\hat{\mathbf{u}}_j\right|},C_{s1}\Delta\right]\quad(8)$$

The model parameters in the SAS source term were: $\kappa=0.41$, $C_{SAS}=2$, $\zeta_2=3.51$, $\sigma_\phi=2/3$ and $C_{s1}=0.262$, while Δ is the grid spacing based on the third root of the control volume.
The original SAS model did not provide sufficient damping of the smallest scales at the grid limit and for a small time step [44]. Here, the WALE model [45] was selected as a HWN damping limit, as it gives $\mu_{t,WALE}=0$ for steady shear flows. This ensures that the RANS model remains unaffected even for relatively coarse grids [44], leading to the following expression for the turbulent viscosity: $\mu_t=\max\left(\mu_{t,SAS},\mu_{t,WALE}\right)$. In the present study the dissipation rate of the turbulence energy was treated as

$$\hat{\epsilon}=C_\mu\hat{\omega}\hat{k}.\quad(9)$$

– LES: The Favre filtered balance equations of mass, momentum, energy and species were solved. The k-equation eddy viscosity sub-grid scale model [71] (hereafter, TKE) and the conventional Smagorinsky model [61] (hereafter, SMAG) are utilized for the closure problem. Both models are based on the SGS kinetic energy $\tilde{k}=\frac{1}{2}\left(\widetilde{\mathbf{u}\cdot\mathbf{u}}-\widetilde{\mathbf{u}}\cdot\widetilde{\mathbf{u}}\right)$, where $\widetilde{\mathbf{u}}$ is the filtered density weighted velocity. The following assumptions for the SGS density weighted stress tensor $\mathbf{B}$ and the filtered deviatoric part of the rate of strain tensor $\widetilde{\mathbf{D}}_D$ are used:

$$\mathbf{B}=\frac{2}{3}\overline{\rho}\tilde{k}\mathbf{I}-2\mu_B\widetilde{\mathbf{D}}_D,\quad(10)$$

$$\widetilde{\mathbf{D}}_D=\left[\widetilde{\mathbf{D}}-\frac{1}{3}\left(\mathrm{tr}\,\widetilde{\mathbf{D}}\right)\mathbf{I}\right],\quad(11)$$

$$\widetilde{\mathbf{D}} = \frac{1}{2}\left(\text{grad}\,\widetilde{\mathbf{u}} + \text{grad}\,\widetilde{\mathbf{u}}^{\mathrm{T}}\right), \tag{12}$$

$$\mu_B = c_k \overline{\rho}\sqrt{\tilde{k}}\Delta, \tag{13}$$

where $\mathbf{I}$ is the unit tensor, ρ the density, μ_B the SGS viscosity and Δ the top-hat filter with a length estimated as the cubic root of the control volume that applied as filter kernel. The subgrid kinetic energy $\tilde{k}$ was estimated by solving a separately modeled transport equation of the form,

$$\frac{\partial \bar{\rho}\tilde{k}}{\partial t} + \frac{\partial \bar{\rho}\tilde{k}\tilde{\mathbf{u}}_j}{\partial x_j} = F_p + F_d - F_\epsilon, \tag{14}$$

$$F_p = -\mathbf{B}\cdot\widetilde{\mathbf{D}}, \tag{15}$$

$$F_d = \frac{\partial}{\partial x_j}\left((\mu_B + \mu)\frac{\partial \tilde{k}}{\partial x_j}\right), \tag{16}$$

$$F_\epsilon = c_\epsilon\, \overline{\rho}\, \tilde{k}^{3/2}/\Delta, \tag{17}$$

where F_p is production, F_d diffusion and F_ϵ dissipation terms, respectively, and $c_k = 0.07$, $c_\epsilon = 1.048$ are model coefficients [52].
The conventional Smagorinsky SGS model can be recovered from (14) by assuming local equilibrium, i.e., $F_p = F_\epsilon$. Thus, the SGS kinetic energy can be computed from the following relation:

$$\mathbf{B}\cdot\widetilde{\mathbf{D}} + c_\epsilon\, \overline{\rho}\, \tilde{k}^{3/2}/\Delta = 0. \tag{18}$$

Using Eq. (10) and introducing the following coefficients,

$$a = \frac{c_\epsilon}{\Delta}, \qquad b = \frac{2}{3}\text{tr}\,\widetilde{\mathbf{D}}, \qquad c = -2c_k\Delta\widetilde{\mathbf{D}}_D\cdot\widetilde{\mathbf{D}},^{1} \tag{19}$$

the relation of Eq. (18) can be reformulated to the model quadratic equation $at^2 + bt + c = 0$, where $t = \sqrt{\tilde{k}}$. The final relation for $\tilde{k}$ can be formulated as

$$\tilde{k} = \left(\frac{-b + \sqrt{b^2 - 4ac}}{2a}\right)^2. \tag{20}$$

The models constants are: $c_k = 0.02$ and $c_\epsilon = 1.048$ [52]. The dissipation rate $\tilde{\epsilon}_{sgs}$ from the SMAG model was expressed according to Eq. 17.
The subgrid fluxes were modeled according to a simple gradient diffusion approximation

$$\mathbf{b}_s = \frac{\mu_B}{\text{Sc}_t}\left(\frac{\partial \tilde{Y}_s}{\partial x_j}\right), \tag{21}$$

$$\mathbf{b}_h = \frac{\mu_B}{\text{Pr}_t}\left(\frac{\partial \tilde{h}}{\partial x_j}\right), \tag{22}$$

where Sc_t and Pr_t are turbulence Schmidt and Prandtl numbers.

[1] Actually, the double inner product is applied: $\widetilde{\mathbf{D}}_D : \widetilde{\mathbf{D}}$

2.2 EDC closure for RANS/URANS and SAS

The Eddy Dissipation Concept is based on the energy cascade model and assumes that molecular mixing and chemical reactions occur on the smaller dissipative eddies, which are close to the Kolmogorov length scales and are termed "fine structures". The characteristic length L^* and velocity u^* scales of the fine structures are of the same order of magnitude as Kolmogorov scales and can be expressed as

$$L^* = \frac{2}{3}\left(\frac{3C_{D2}^3}{C_{D1}^2}\right)^{1/4}\left(\frac{\nu^3}{\hat{\epsilon}}\right)^{1/4}, \tag{23}$$

$$u^* = \left(\frac{C_{D2}}{3C_{D1}^2}\right)^{1/4}(\nu\hat{\epsilon})^{1/4}, \tag{24}$$

where $\nu = \mu/\rho$ is the kinematic viscosity, $C_{D1} = 0.134$ and $C_{D2} = 0.5$ [16]. Here, we assume that the full cascade takes place at each numerical cell, and the connection between the fine structure and the larger eddies is achieved through the cascade. Thus, characteristics of the large eddies such as velocity u' can be evaluated using the turbulence model. The turbulence kinetic energy $\hat{k}$ and its dissipation were found from the relevant solved transport equation in RAS and SAS.

In the model expressed below, different superscripts refer to states inside fine structures (*), surroundings ($\circ$) and mass-weighted values of the computational cell ($\wedge$).

In this study, the ratio between the mass in the fine structures and the total mass was taken as

$$\gamma^* = \left(\frac{u^*}{u'}\right)^2 = \left(\frac{3C_{D2}}{4C_{D1}^2}\right)^{1/2}\left(\frac{\nu\hat{\epsilon}}{\hat{k}^2}\right)^{1/2}, \tag{25}$$

as suggested by Magnussen [39].

The mass exchange between the fine structures and the surroundings, divided by the mass of the fine structures, is defined as

$$\dot{m}^* = 2\frac{u^*}{L^*} = \left(\frac{3}{C_{D2}}\right)^{1/2}\left(\frac{\hat{\epsilon}}{\nu}\right)^{1/2}. \tag{26}$$

The mass-averaged reaction rate for the s-th species is given as

$$-\omega_s = \frac{\bar{\rho}\gamma^*\dot{m}^*\chi}{1-\gamma^*\chi}\left(\hat{Y}_s - Y_s^*\right),\ s = 1, \ldots, N_s, \tag{27}$$

and the relationship between the mass-averaged mean state, fine-structure state and surrounding state is expressed as

$$\hat{\Psi} = \gamma^*\chi\Psi^* + (1-\gamma^*\chi)\Psi^\circ. \tag{28}$$

Here, χ is the reacting fraction of the fine structures, which can depend on probability of co-existence of the reactants, degree of heating and a limiter to

the reaction due to lack of reactants. In the present study, $\chi = 1$, as suggested by Gran and Magnussen [19]. The mass fraction $\hat{Y}_s$ for species s was calculated from solving the species mass transport equation for each individual species. Turbulence diffusion of energy and species mass were modeled with the turbulence viscosity and turbulence Prandtl and Schmidt numbers, Pr_t and Sc_t. The fine-structure mass fraction Y_s^* was computed through the detailed chemistry approach.

2.3 EDC closure for LES

It is worth noting that the model formulations discussed in previous subsection have been developed for the conventional RANS/URANS approach. In the authors' previous study [35], this formulation was adopted for the large-eddy simulation in its logical choice, Eq. 27 was used to calculate the filtered reaction rate, $\bar{\omega}$. This formulation was used in the present study. Also, it should be mentioned that this closure is suitable for most practical LES grid sizes (i.e. $\Delta > \delta_{th}$ [7]), as in the EDC combustion predominantly takes place in the fine structures at the sub-grid level. Here, δ_{th} is the thermal flame thickness, which can estimated as [7]: $\delta_{th} = 2\delta_z \left(1+\tau\right)^{0.7}$, where δ_z is the Zel'dovich flame thickness and τ is the modified heat release parameter.

However, to complete formulation, the closure should have the correct behavior for the very fine grids, when the filter width approaches the Kolmogorov scales. It is worth noticing that for combustion, LES will hardly become DNS (Direct Numerical Simulation), since only fluid scales are resolved, whereas chemical scales can be much smaller. For this purpose, Eq. 27 can be modified by adding the blending function, f_b, in the spirit of Butz et al. [7] as

$$f_b = \exp\left[-0.7\left(\frac{\Delta}{\delta_{th}}\right)^{1/7}\right]. \tag{29}$$

The final formulation for the filtered reaction rate can be expressed as:

$$-\bar{\omega}_s = \frac{\bar{\rho}\gamma^*\dot{m}^*\chi}{1-\gamma^*\chi}\left(\tilde{Y}_s - Y_s^*\right)\left[1-f_b\right] + \omega_s^* f_b,\ s = 1,\ldots,N_s. \tag{30}$$

It worth noting that another limiting case can be considered when all turbulent motions are resolved but not the inner flame structure. However, in this case the present formulation is not expected to predict the overall behavior of a laminar filtered flame front.

2.4 The finite-rate chemistry approach

Finite-rate chemical kinetics was taken into account by treating the fine structures as constant pressure and adiabatic homogeneous reactors. Thus, the fine

structures mass fractions values Y_s^* can be calculated by solving a system of ODEs describing a transient Perfectly Stirred Reactor (PSR) [19],

$$\frac{dY_s^*}{dt} = \frac{\omega_s^*}{\rho^*} + \frac{1}{\tau^*}\left(Y_s^\circ - Y_s^*\right),\ s = 1, \ldots, N_s. \tag{31}$$

The reaction rate ω_s^* was evaluated from a chemical kinetics mechanism. Y_s° is the mass fraction of the inflow stream to the reactor (cf. Eq. 28). In the present study, it was assumed adiabatic and isobaric PSRs. The solution of Eq.31 was achieved by integrating it in timescale $[0, \tau_{lim}]$, where τ_{lim} is the limiting value, which estimation is discussed in Sec. 2.5.1. The fine structures mass fractions were used as initial conditions to close the initial value problem. The residence or mixing time scale τ^* was evaluated using the relation $\tau^* = 1/\dot{m}^*$.

2.5 Calculation of ω_s^*

The net source of the chemical species due to reactions ω_s^* from Eq. 31 is calculated as the sum of the N_s Arrhenius reactions that the species participates in:

$$\omega_s^* = \mathcal{M}_s \sum_{r=1}^{N_s} \left(\nu_{s,r}'' - \nu_{s,r}'\right) \hat{\mathrm{R}}_{s,r}, \tag{32}$$

where $\mathcal{M}_s$ is the molar mass of species s and $\hat{\mathrm{R}}_{s,r}$ is the Arrhenius molar rate of formation of species s in reaction r.

The Arrhenius molar rate is evaluated according to the following expression:

$$\hat{\mathrm{R}}_{s,r} = k_{\mathrm{f},r} \prod_{j=1}^{N} \left[\frac{\rho Y_j}{\mathcal{M}_j}\right]^{\nu_{j,r}^{'}} - k_{\mathrm{b},r} \prod_{j=1}^{N} \left[\frac{\rho Y_j}{\mathcal{M}_j}\right]^{\nu_{j,r}^{''}}, \tag{33}$$

where $\nu_{j,r}^{'}$ is the rate exponent for reactant species j in reaction r and $\nu_{j,r}^{''}$ represents the rate exponent for product species j in reaction r, $k_{\mathrm{f},r}$ and $k_{\mathrm{b},r}$ are the forward and backward rates coefficients for reaction r.

The r-th reaction is considered according to

$$\sum_{s=1}^{N} \nu_{s,r}^{'} \mathrm{A}_s \underset{\mathrm{k_{b,r}}}{\overset{\mathrm{k_{f,r}}}{\rightleftarrows}} \sum_{s=1}^{N} \nu_{s,r}^{''} \mathrm{A}_s, \tag{34}$$

where N is number of species in the chemical mechanism, $\nu_{s,r}^{'}$ is stoichiometric coefficient for reactant s in reaction r, $\nu_{s,r}^{''}$ is stoichiometric coefficient for product s in reaction r, while A_s denotes species s.

For the irreversible reaction r, the forward reaction coefficient $k_{\mathrm{f},r}$ is calculated according to the Arrhenius expression

$$k_{\mathrm{f},r} = A_r T^{\beta_r} \exp\left(\frac{-T_{ar}}{T}\right), \tag{35}$$

where A_r, β_r and T_{ar} are constants.

For the reversible reaction r, the backward reaction coefficient is calculated according to

$$k_{\mathrm{b},r} = \frac{k_{\mathrm{f},r}}{K_r}, \tag{36}$$

where K_r is the equilibrium coefficient,

$$K_r = \exp\left[\frac{\Delta S_r}{R} - \frac{\Delta H_r}{RT}\right]\left[\frac{P_{atm}}{RT}\right]^{\sum_{s=1}^{N}\left(\nu''_{s,r}-\nu'_{s,r}\right)}, \tag{37}$$

where $P_{atm} = 101325$ Pa is the ambient pressure and R represents the universal gas constant. The change of the Gibbs free energy is given by

$$\frac{\Delta S_r}{R} = \sum_{s=1}^{N}\left(\nu''_{s,r} - \nu'_{s,r}\right)\frac{S_s}{R}, \tag{38}$$

$$\frac{\Delta H_r}{R} = \sum_{s=1}^{N}\left(\nu''_{s,r} - \nu'_{s,r}\right)\frac{h_s}{R}, \tag{39}$$

where S_s and h_s are the molar entropy and enthalpy of the species s calculated at temperature T and the atmospheric pressure.

2.5.1 Integration of the PSRs in time

The integration of Eq. 31 in time is one of the unresolved issues of the present model. For the steady state flow (assuming the RANS approach), it does not matter if the PSR is integrated to(wards) infinity. For a transient flow, there is a question of which timescale that should limit the PSR integration time. In the present work, the additional time scale τ_{lim} has been introduced and the fixed value of τ_{lim} was used to integrate equations in the PSR at the timescale of $[0, \tau_{\mathrm{lim}}]$. The value $\tau_{\mathrm{lim}} = 10$ s most likely assumes that the PSR is integrated to the steady-state.

However, in general, it does not appear meaningful to integrate the PSR longer than the existence of the structures it represents. Another important aspect is that τ_{lim} plays a crucial role for the overall computational time. On the one hand, calculations of the finite-rate chemistry take more than 70% from the total computational time. On the other hand, the under-estimated value of τ_{lim} may lead to numerical instabilities and final solution divergence.

For all the present simulations, a formulation based on the local residence time of the PSR has been applied

$$\tau_{\mathrm{lim}} = \min\left[10, 3 \cdot \max\left(\tau_{Kn}, \tau_n^*\right)\right], \tag{40}$$

where τ_{Kn} and τ_n^* are the local Kolmogorov time and the PSR residence time in the cell n.

2.5.2 Kinetics schemes

For the propane/air combustion the following chemical mechanisms were used:

– the global one-step (hereafter GLB1) [68], [69]:

$$\mathrm{C_3H_8} + 5\,\mathrm{O_2} \longrightarrow 3\,\mathrm{CO_2} + 4\,\mathrm{H_2O}; \tag{41}$$

– the global three-step mechanism (hereafter GLB3) constructed in the spirit of Sabelnikov and Fureby [51]:

$$\begin{array}{ccc} \mathrm{C_3H_8} + 3.5\,\mathrm{O_2} & \longrightarrow & 3\,\mathrm{CO} + 4\,\mathrm{H_2O} \\ \mathrm{CO} + 0.5\,\mathrm{O_2} & \rightleftarrows & \mathrm{CO_2} \\ \mathrm{O_2} + \mathrm{N_2} & \longrightarrow & 2\,\mathrm{NO}; \end{array} \tag{42}$$

– the full San-Diego mechanism [53] (hereafter SD);
– the full GRI-3.0 mechanism [6] (hereafter GRI3).

It should be noticed that the parameters of GLB3 from [51] were adjusted to those shown in Table 1. The original parameters gave very low values of O2 in our calculations and correspondingly large values of NO. The changes were made by comparison with SD.

The reaction rate of Eq. 41 can be expressed as

$$\frac{\omega_{\mathrm{C3H8}}}{\mathcal{M}_{\mathrm{C3H8}}} = -A \left(\frac{\rho Y_{\mathrm{C3H8}}}{\mathcal{M}_{\mathrm{C3H8}}} \right)^{n_{\mathrm{C3H8}}} \left(\frac{\rho Y_{\mathrm{O_2}}}{\mathcal{M}_{\mathrm{O_2}}} \right)^{n_{\mathrm{O_2}}} T^{\beta_i} \exp\left[\frac{-T_{a,i}}{T} \right], \tag{43}$$

and similarly for the reactions of Eq. 42. The constants are provided in Table 1.

Table 1 Reaction constants for the global mechanisms

i	A_i (m, kg, kmol, s)	β_i	T_{ai} (K)	n_{C3H8}	n_{O2}	n_{CO}	n_{N2}
41	4.836×10^9	0	15100	0.1	1.65		
42.1	3.62×10^9	0.93	18590	0.36	1.75		
42.2	2.14×10^6	0.87	12710		0.83	0.55	
42.3	1.40×10^{10}	−0.3	38440		1		1

2.6 Turbulent Flame Closure (TFC) Model

The following balance equation was used for the density-weighted mean combustion progress variable $\hat{c}$:

$$\frac{\partial \bar{\rho}\hat{c}}{\partial t} + \frac{\partial \bar{\rho}\hat{u}_j\hat{c}}{\partial x_j} = \frac{\partial}{\partial t}\left(\frac{\mu_t}{\mathrm{Sc}_t} \frac{\partial \hat{c}}{\partial x_j} \right) + \rho_u U_t \mid \bigtriangledown \hat{c} \mid . \tag{44}$$

Here, x_j and u_j are the coordinates and flow velocity components, respectively. μ_t is the turbulence viscosity and Sc_t represents turbulence Schmidt number.

The progress variable is defined as a normalized sum of the product species mass fractions

$$c = \frac{\sum_k a_k \left(Y_k - Y_k^u\right)}{\sum_k a_k Y_k^{eq}} = \frac{Y_c}{Y_c^{eq}}, \tag{45}$$

where superscript u denotes the unburnt reactant, Y_k denotes the k^{th} species mass fraction, superscript eq denotes chemical equilibrium and a_k denotes constants that are typically zero for reactants and unity for a few product species.

The Zimont turbulent flame speed closure [72] (hereafter, TFC) was computed as

$$U_t = Au' \left(\frac{\tau_t}{\tau_c}\right)^{1/4}, \tag{46}$$

where $A = 0.52$ is the model constant, u' is the root-mean-square velocity, α is the unburnt thermal diffusivity, l_t is the turbulence length scale, $\tau_t = l_t/u'$ is the turbulence time scale, $\tau_c = \alpha/U_l^2$ is the chemical time scale and U_l is the laminar flame speed. The turbulence length scale was computed according to $l_t = C_D \left(u'\right)^3/\epsilon$, where $C_D = 0.37$.

The original TFC model (Eqs. 44, 46) [27], [72] did not incorporate chemical kinetics but assumed that the influence of chemistry on a turbulent premixed flame may be qualitatively approximated the correct laminar flame speed, which depends on the chemistry. However, in the present study a simple combination of TFC and the β-PDF approach with the equilibrium chemistry assumption [64], as implemented in the CFD code Ansys Fluent (AF), was used for taking into account chemical effects. Here, strictly following the AF implementation transport equations for the mean reaction progress variable, $\hat{c}$, mean mixture fraction, $\hat{f}$ and its variance, $\widehat{f'^2}$ were solved. It is supposed that ahead of the flame ($c = 0$), the fuel and oxidizer are mixed but unburnt, and behind the flame ($c = 1$), the mixture is burnt. Since the present cases were fully premixed, the mixture fraction should become a constant and its variance zero. Therefore, these formulations of the model are not included here.

In the present study a chemical equilibrium assumption is used, where reactions rates are sufficiently fast for the mixture to be in a state of chemical equilibrium. With this assumption the equilibrium state of density, temperature and composition can be obtained by minimizing the free energy [64].

Density-weighted mean scalars (species fractions and temperature), denoted by $\hat{\phi}$ are calculated from the probability density function (PDF) as

$$\hat{\phi} = \int_0^1 \int_0^1 \phi\left(f, c\right) p\left(f, c\right) df dc. \tag{47}$$

Using assumption of thin flames, the mean scalars are determined from

$$\hat{\phi} = \hat{c} \int_0^1 \phi_b\left(f\right) p\left(f\right) df + \left(1 - \hat{c}\right) \int_0^1 \phi_u\left(f\right) p\left(f\right) df, \tag{48}$$

where the subscripts b and u denote burnt and unburnt, respectively.

Here, again for the fully premixed cases, integration over the mixture fraction should be for the constant value only. The further aspects are provided in the AF documentation [2].

2.7 Radiation

The radiation was treated by the P1-approximation [9]. The weighted-sum-of-gray-gases-model (WSGGM) [62] was used to calculate gas phase absorption/emission. In the present study, a new function has been implemented to calculate the mean beam lengths for optically thin media, L_0, as $L_0 = 4V/A$, where A is the entire area bounding the volume V. These lengths are often called geometric mean beam lengths, based on the work by Dunkle [13]. Further details of the mathematical apparatus were provided in the previous studies [34], [35].

3 Numerical aspects

The main emphasis of this work was put on the problem of validation of the Eddy Dissipation Concept implemented in the OpenFOAM (hereafter OF) toolbox [67]. However, to investigate the influence of the heat losses to the flame-holder, some calculations have been carried out based on the premixed TFC model together with the conjugate fluid-solid heat transfer using the Ansys Fluent (hereafter AF) [2]. It is worth noticing that the same grid was used for both solvers.

3.1 OpenFOAM

The edcPisoFOAM solver has been developed based on the OpenFOAM code [67]. The solver employs the unstructured finite-volume method and the PISO (pressure implicit with splitting of operators) algorithm [63] for the pressure-velocity coupling, implemented according to Rhie and Chow type interpolation for the cell-centered data storage structure [23].

The numerical method had second-order accuracy in space and time. The linear-upwind interpolation scheme (the second-order upwind scheme [65]) and linear (second-order central differences, CDS-2) interpolation were applied for convective terms approximation and other spatial derivatives, respectively, for the RAS calculations. For the Scale-Adaptive and Large-Eddy simulations, the total variation diminishing (TVD) [21] and normalized-variable (NVD) [24] schemes were used for the scalars to avoid unphysical overshoots and second law violations. A second-order implicit Euler method (BDF-2 [17]) was used for time integration together with the dynamic adjustable time stepping technique to guarantee a local Courant number less than 0.75 for URANS, SAS and LES.

The calculation of the species reaction rate requires the integration of Eq. 31 for each computational cell in the domain. For this purpose, the robust LSODA algorithm [48] was used. Some results of the detailed validation and verification study of the new integrator are provided in Appendix A. The relative tolerance, absolute tolerance and maximum number of iterations to meet the target accuracy were set to 10^{-5}, 10^{-5} and 10^3, respectively.

OpenFOAM is the massive parallel open source C++ classes library based on message-passing interface (MPI). The present calculations were carried out at the Vilje high performance computing (HPC) facility (https://www.sigma2.no/content/vilje), which is a distributed memory system that consists of 1440 nodes interconnected with a high-bandwidth low-latency switch network (FDR Infiniband). Each node has two 8-core Intel Sandy Bridge (2.6 GHz) and 32 GB memory. Most present calculations performed using 128 and 256 cores in parallel. Typical calculation time for one time step in reactive simulations varied between $10 - 20$ s, and the total (effective) simulation time per run took around two weeks.

3.2 Ansys Fluent

Using the factorized finite-volume method, the steady, incompressible Navier-Stokes equations were solved with a second-order accuracy in space and time. The velocity and pressure fields were matched with a centered computational template based on the SIMPLEC [63] algorithm within the spirit of Rhie and Chou [49]. The convective terms were represented according to the second-order upwind scheme (SOU) [65].

4 Test cases description

4.1 Experimental set up

The description of the Volvo test rig and relevant experimental data was provided in [58], [59], [60]. Fig. 1 shows a schematic drawing of the test section. The set-up consisted of a straight channel with a rectangular cross-section, divided into an inlet section length 0.5 m and a channel passage section length $L = 1$ m and 0.12 m $\times$0.24 m cross-section. The inlet section was used for flow straightening and turbulence control. The air entering the inlet section was distributed over the cross-section by a critical plate that, at the same time, isolated the channel acoustically from the air supply system. The channel passage section ended in a circular duct with a large diameter. The triangular bluff-body (with side length, $H = 0.04$ m) was mounted with its reference position 0.681 m upstream of the channel exit. The principal flow parameters and experimental conditions are summarized in Table 2 for non-reactive and reactive (propane is fuel) cases, where Re is the Reynolds number based on the bluff-body side length, St is the Strouhal number, U is velocity, T is temperature, p is the static pressure, ϕ is the equivalence ratio and L_r/H represents

the recirculation zone length. The symbol ∞ denotes that a parameter is applied at the rig inlet. The laminar flames speeds for the reacting cases C1 and C2 were set as $S_l = 0.14$ m/s and $S_l = 0.77$ m/s, respectively.

The critical remark should be done here related to estimation of the adiabatic flame temperatures since two sets of experiments were performed: using the CARS measurements [60] and the gas analysis [58]. Sjunnesson et al. [60] provided the adiabatic temperatures for the CARS measurements ($\phi = 0.58 - 0.61$) as $T_{ad} = 1713$ K and $T_{ad} = 1876$ K for the cases C1 and C2, respectively. However, all present numerical results were calculated for the conditions with $\phi = 0.65$ relevant to the gas measurements [58]. The estimated adiabatic temperatures for the cases C1, C2 and $\phi = 0.65$ were $T_{ad} = 1800$ K and $T_{ad} = 2035$ K, respectively, which are used in next sections for all figures to normalize temperature. The calculated adiabatic temperatures were consistent with the temperatures calculated on the basis of chemical equilibrium assumption (T_{eq}) as well. Table 3 summaries all these findings.

Table 2 Flow parameters used for the Volvo rig: inert (C0) and reactive (C1-C2) cases

ID	Re	U_∞ [m/s]	T_∞ [K]	p_∞ [kPa]	ϕ	ϕ, CARS	L_r/H	St
C0	45,000	16.6	300	101	-	-	1.33	0.25
C1	47,000	17.3	300	101	0.65	0.61	3.55	-
C2	28,000	37.7	600	101	0.65	0.58	3.16	-

Table 3 Adiabatic and chemical equilibrium flame temperatures for $C1$ and $C2$ flow conditions

	Experiment, CARS	Present calculations			
	T_{ad} [K]	T_{ad} [K]	T_{eq} [K]	T_{ad} [K]	T_{eq} [K]
ID	$\phi = 0.58 - 0.61$	$\phi = 0.6$	$\phi = 0.6$	$\phi = 0.65$	$\phi = 0.56$
C1	1713	1707	1707	1801	1800
C2	1876	1944	1942	2035	2031

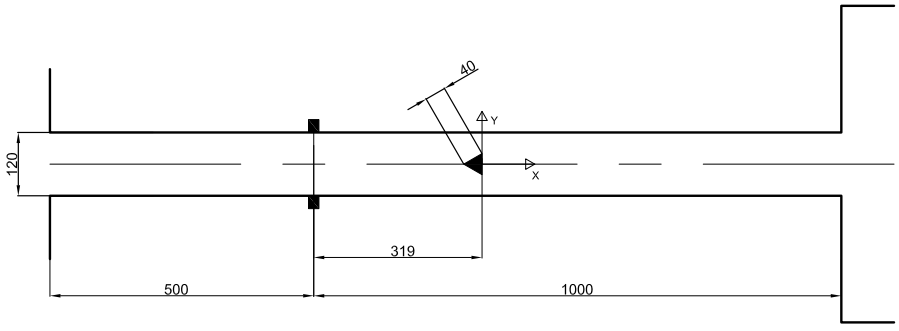

Fig. 1 The sketch of the Volvo test rig. All linear dimensions are in mm

4.2 Computational domain and grids

4.2.1 The RAS grid

The two-dimensional computational domain is presented in Fig. 2 and consisted of an inlet buffer domain (size of 0.2 m × 0.24 m) and a channel passage (size of 1.5 m × 0.12 m). It was decided to attach an inlet buffer domain to the main computational area, allowing the inlet velocity and temperature profiles to form implicitly during computations [31]. The integration domain was split into three blocks to generate a high-quality unstructured quad/triangular mesh:

- the inlet buffer and a part of the channel without bluff-body. The channel part was resolved with 135 and 45 nodes in the horizontal and vertical directions, respectively, with exponential grading of cells towards the bluff body;
- the central part of the channel passage with size of 0.2 m × 0.12 m, including the obstacle, as described in Fig. 2,(a). The bluff body edges contained 90 grid points, while the horizontal and vertical sides of the domain were resolved with 75 and 45 nodes, respectively, to obtain smooth mesh transition towards the flame holder;
- the remaining downstream part of the channel with resolution of 135 and 45 in the horizontal and vertical directions, respectively, with exponential decreasing of nodes towards the outlet.

The viscous boundary layers were attached to the obstacle and the channel walls. The first element length, the growth factor and the total number of rows were set to 10^{-5} m, 1.2 and 11, respectively, for the triangular cylinder and 5×10^{-4} m, 1.2 and 5, respectively, for the channel walls. The distribution of the non-dimensional distance to the wall y^* was about 1 both for the obstacle and the channel walls. Hereafter, this grid has label M1.

4.2.2 The grid for SAS and LES

The computation domain and the unstructured mesh (hereafter, this grid has label M2) is shown in Fig. 3. The mesh was refined in the vicinity of the bluff body in order to resolve properly the separation of laminar boundary layers. A total number of 2.2 million grid points were used in conjunction with three grid blocks.

The integration domain was split into three blocks to generate the unstructured hexahedral/tetrahedral mesh:

- the inlet channel without bluff-body. The channel part was resolved with $135 \times 70 \times 45$ nodes in the stream-wise, transverse- and span-wise directions, respectively, with exponential grading of cells towards the bluff body;
- the central part of the channel passage including the obstacle with size of 0.2 m × 0.12 m (Fig. 3,(b)). The bluff body edges were discretized by 75 grid points, while the stream-wise, transverse and span-wise sides of

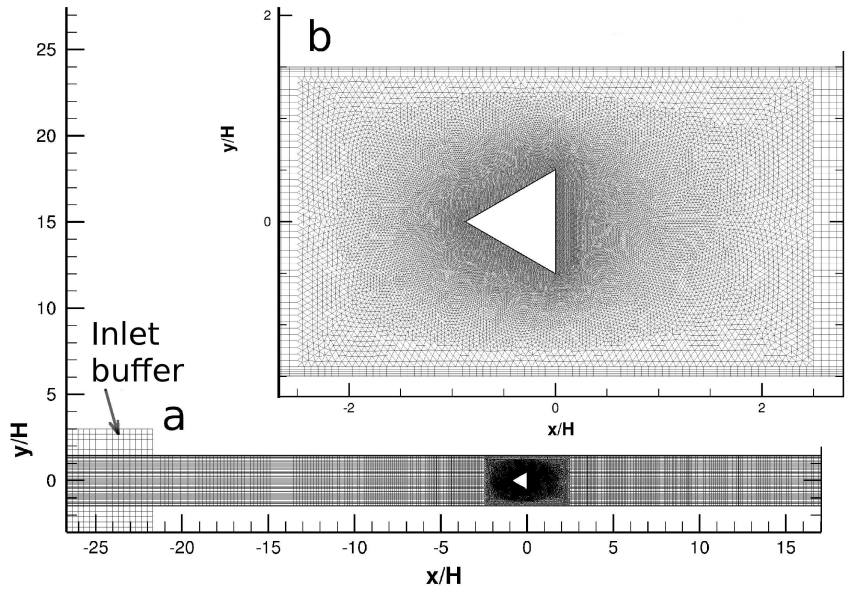

Fig. 2 The general view of the computational domain for RANS/URANS (a), zoom of the grid (b) at the vicinity of the bluff-body. Here, x and y are the domain coordinates in stream-wise and transverse directions, according to the scheme on Fig. 1

the domain were resolved with $80 \times 70 \times 45$ nodes, respectively, to obtain smooth mesh transition towards the flame holder;
- the remaining downstream part of the channel with resolution of $135 \times 70 \times 45$ nodes with exponential decreasing of nodes towards the outlet.

The viscous boundary layers were attached to the obstacle and the channel walls. The first element length, the growth factor and the total number of rows were set to 10^{-4} m, 1.15 and 7, respectively, for the triangular cylinder and 10^{-4} m, 1.25 and 13, respectively, for the channel walls. The average distributions of the non-dimensional distance to the wall y^* were 4.6 and 5.4 for the obstacle and the channel walls, respectively.

4.2.3 Grid dependence study

The present RAS results were obtained using two sets of grids: a low-resolution grid and a high resolution grid. The high-resolution grid was created by simple refinement of the low-resolution grid by a factor of 2×2 in the horizontal and vertical directions as well as the flame holder. The details of the high-resolution grid was provided above. In general, the differences between the two sets of grids were insignificant (with 5% difference) for the mean velocity and temperature.

The grid dependence study for the SAS and LES calculations was carried out using the refined grid (hereafter, M3). For this case, the M2 grid was

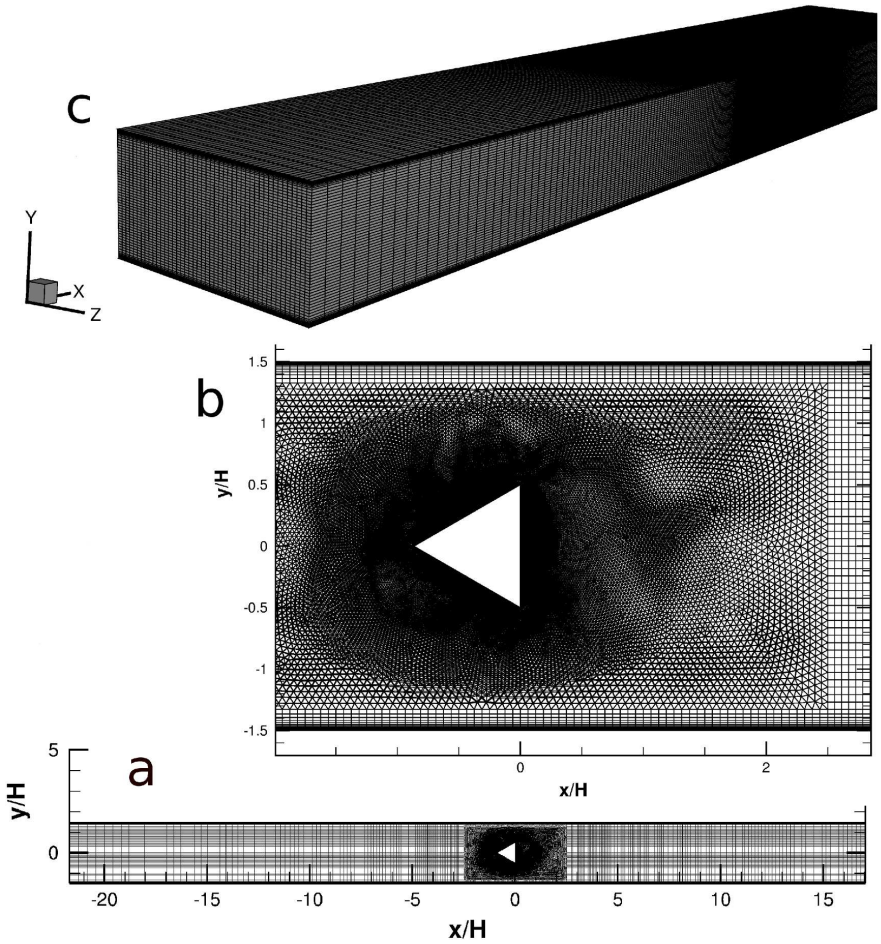

Fig. 3 Details of the SAS and LES grid: description of the grid in x-y (a), zoom of the grid in x-y plane at the vicinity of the bluff-body and general view of the grid (c). Here, x, y and z are the domain coordinates in stream-wise, transverse and span-wise directions, according to the scheme on Fig. 1

simply adapted by a factor of 1.4 leading to the total number of cells about of 4.7 M.

4.3 Boundary conditions

The inflow velocity, temperature and turbulence properties were specified based on the experimental settings. The inflow turbulence level was set to 3%. Constant values for inlet velocity and temperature (according to Table 2) were set for the URANS simulations. For the SAS and LES calculations the inlet velocity and temperature profiles were extracted and interpolated from

the URANS predictions at the location $x/H = -2$. A zero-gradient pressure boundary was applied for all inflow boundaries, while the pressure at the outlet was specified to 101 kPa. The inlet values for the turbulence dissipation, $\hat{\epsilon}$, and specific dissipation, $\hat{\omega}$, were set according to the simple assumptions $\hat{\epsilon} = {C_\mu}^{0.75}\hat{k}^{1.5}L_m^{-1}$, $\hat{\omega} = \hat{k}^{0.5}{C_\mu}^{-0.25}L_m^{-1}$, where C_μ is the constant $C_\mu = 0.09$ and L_m is the mixing length, which was set to the constant value $L_m = 0.025$ m. A non-slipping condition for velocity was applied to the walls. The turbulence kinetic energy was set to the fixed small value of 10^{-12} m^2/s^2 at all walls, while the wall-functions for $\hat{\epsilon}$ and $\hat{\omega}$ were used for the RAS and SAS models. The propane/air mixture was specified in terms of the species mass fractions. Zero-gradient diffusion boundary conditions were applied for species at the walls. The symmetry conditions were imposed at the lateral boundaries. Temperature boundary conditions at solid walls was treated according to the zero-gradient assumption. For RANS/URANS calculations also isothermal walls and the conjugate fluid-solid heat transfer were applied, as specified in Table 4.

In the present SAS and LES simulations, the slip boundary condition was applied to the channel walls (which may be considered as a simplistic representation of flame quenching due to heat losses [36]), since these calculations were focused on the models performance at the core central region of the flow.

The reason for not adding perturbations at the inlet for SAS and LES calculations was the same as discussed earlier [32]: In the designed grid, the inflow perturbations will be highly damped due to grid expansion from the surface of the bluff-body towards the inlet boundary, and the probability that these perturbations will reach the triangular cylinder is small.

5 Results

5.1 Overview

All simulated cases are listed in Table 4, where the following abbreviations are used: Code – the computational code: Ansys Fluent (AF) or OpenFOAM (OF), M – mesh: according to Sec. 4.2, N – convective schemes: the second-order upwind (SOU), the normalized-variable diagram (NVD) (γ), the total variation diminishing (TVD), CF – flow conditions: according to Table 2, TR – the approach for solution of the Navier-Stokes equations, (U)RANS , SAS or LES, TM – turbulence model: k-ϵ (SKE), k-ω SST (SST), k-equation eddy-viscosity sub-grid scale model (TKE), Smagorinsky (SMAG), TCM – turbulence-chemistry interaction model: Eddy Dissipation Concept (EDC), Turbulent Flame Closure (TFC), CH – chemistry mechanism: according to Sec. 2.5.2, R – radiation sub-model: P1 or none, Sc_t – turbulence Schmidt number, Pr_t – turbulence Prandtl number, T_{wo} and T_{wc} – temperature boundary conditions for the obstacle and channel walls, respectively: zero-gradient (zg), isothermal (T_{isoth} = 300 K and T_{isoth} = 600 K for cases C1 and C2, respectively) or conjugate fluid-solid heat transfer (CHT).

Table 4 Run matrix for the Volvo test rig

Run	Code	M	N	CF	TR	TM	TCM	CH	R	Sc_t	Pr_t	T_{wo}	T_{wc}
URANS1	OF	M1	SOU	C1	URANS	SKE	EDC	GLB1	–	0.4	0.85	zg	zg
URANS2	OF	M1	SOU	C1	URANS	SKE	EDC	GLB3	–	0.4	0.85	zg	zg
URANS3	OF	M1	SOU	C1	URANS	SKE	EDC	GRI3.0	–	0.4	0.85	zg	zg
URANS4	OF	M1	SOU	C1	URANS	SKE	EDC	SD	–	0.4	0.85	zg	zg
RANS1	AF	M1	SOU	C1	RANS	SKE	TFC	EQUI	–	0.85	0.85	zg	zg
RANS2	AF	M1	SOU	C1	RANS	SKE	TFC	EQUI	P1	0.85	0.85	CHT	T_{isoth}
RANS3	AF	M1	SOU	C1	RANS	SKE	TFC	EQUI	P1	0.4	0.85	CHT	T_{isoth}
RANS7	AF	M1	SOU	C1	RANS	SKE	TFC	EQUI	–	0.4	0.85	zg	zg
URANS5	OF	M1	SOU	C1	URANS	SKE	EDC	GLB1	P1	0.4	0.85	T_{isoth}	T_{isoth}
RANS4	AF	M1	SOU	C2	RANS	SKE	TFC	EQUI	P1	0.4	0.85	CHT	T_{isoth}
RANS5	AF	M1	SOU	C2	RANS	SKE	TFC	EQUI	P1	0.85	0.85	CHT	T_{isoth}
RANS6	AF	M1	SOU	C2	RANS	SKE	TFC	EQUI	–	0.85	0.85	zg	zg
URANS6	OF	M1	SOU	C2	URANS	SKE	EDC	GLB1	P1	0.85	0.85	T_{isoth}	T_{isoth}
URANS7	OF	M1	SOU	C2	URANS	SKE	EDC	SD	P1	0.85	0.85	T_{isoth}	T_{isoth}
SASI1	OF	M2	TVD	C0	SAS	SST	–	–	–	–	–	zg	zg
SASI2	OF	M2	γ	C0	SAS	SST	–	–	–	–	–	zg	zg
SASI3	OF	M3	γ	C0	SAS	SST	–	–	–	–	–	zg	zg
SASR1	OF	M2	TVD	C1	SAS	SST	EDC	GLB1	–	0.4	0.85	zg	zg
SASR2	OF	M3	TVD	C1	SAS	SST	EDC	GLB1	–	0.4	0.85	zg	zg
LESI1	OF	M3	TVD	C0	LES	TKE	–	–	–	–	–	zg	zg
LESI2	OF	M3	TVD	C0	LES	SMAG ($C_s = 0.1$)	–	–	–	–	–	zg	zg
LESI3	OF	M3	TVD	C0	LES	SMAG ($C_s = 0.053$)	–	–	–	–	–	zg	zg
LESR1	OF	M2	TVD	C1	LES	TKE	EDC	GLB1	–	0.4	0.85	zg	zg
LESR2	OF	M2	TVD	C1	LES	SMAG ($C_s = 0.053$)	EDC	GLB1	–	0.4	0.85	zg	zg
LESR3	OF	M3	TVD	C1	LES	TKE	EDC	GLB1	–	0.4	0.85	zg	zg
LESR4	OF	M2	TVD	C1	LES	SMAG ($C_s = 0.1$)	EDC	GLB1	–	0.4	0.85	zg	zg

For a quantitative validation of the present SAS and LES simulations, the averages have been obtained from the computational results by sampling over 40 vortex shedding periods (N_{vs}) for the SAS non-reactive solution and three flow-through times for the combustion SAS and LES. The flow-through time was defined as the ratio between the axial length of the computational domain to the jet bulk velocity. The hat, the tilde and the bar marks denoting Favre-averaging, filtering Favre-averaging and Reynolds-averaging were omitted for simplicity.

5.2 SAS non-reacting flow results

This section will focus on validation of the non-reactive SAS model. Details of validation and verification of non-reactive RAS and LES were provided previously [31],[32],[33] and are not discussed here. Effects of the SGS models on the LES of the inert flow are briefly discussed in Appendix B.

Figure 4 shows the measured and predicted mean stream-wise velocity and its fluctuation as well as the normalised turbulence kinetic energy along the central-line behind the obstacle. For the sake of completeness, besides the experimental results by Sjunnesson et al. [59], the LDV data by Sanquer et al. [54], who had investigated inert bluff-body wakes as well as premixed bluff-body combustion, were added to the plot. Also, the authors' previous URANS results [31] were included to compare, as well as LES and DES results published by Hasse et al. [22]. Three inert SAS cases have been carried out. SASI1 and SASI2 cases differed only by the applied discretization schemes for convective terms, TVD vs. NVD. The SASI3 case was calculated using the Gamma scheme as well, to check the influence of the grid resolution. In their computations, Hasse et al. [22] utilized the Ansys CFX solver and the CDS-2 scheme for LES, and a bounded second order upwind biased discretization scheme for DES.

Overall, there was a good match between numerical and experimental data. One can observe the same trends between all numerical runs for the axial distribution of the mean stream-wise velocity. Meanwhile, the SASI3 case provided the best result for the stream-vise rms velocity. The normalised turbulence kinetic energy, $K_n = \sqrt{4/3k}/U_\infty$, where the turbulence kinetic energy $k = 3/4\left(u'^2 + v'^2\right)$, is shown in Fig. 4,c. Results from SASI1 and SASI2 predicted quite good the measured turbulence kinetic energy in the near wake (up to $x/H = 2$), while over-predicting it afterwards. In contrast, the SASI3 case matched well the kinetic turbulence energy in the far wake, while under-predicting it in the near wake.

The difference between measurements and numerical calculations for the mean recirculation zone length $< L_r >$ is significant and often subject to discussion. By definition, the recirculation length $< L_r >$ corresponds to the distance between the base of the triangular cylinder and the sign change of the centerline mean stream-wise velocity. The quality of $< L_r >$ predictions may be considered as the deciding factor about the agreement between the

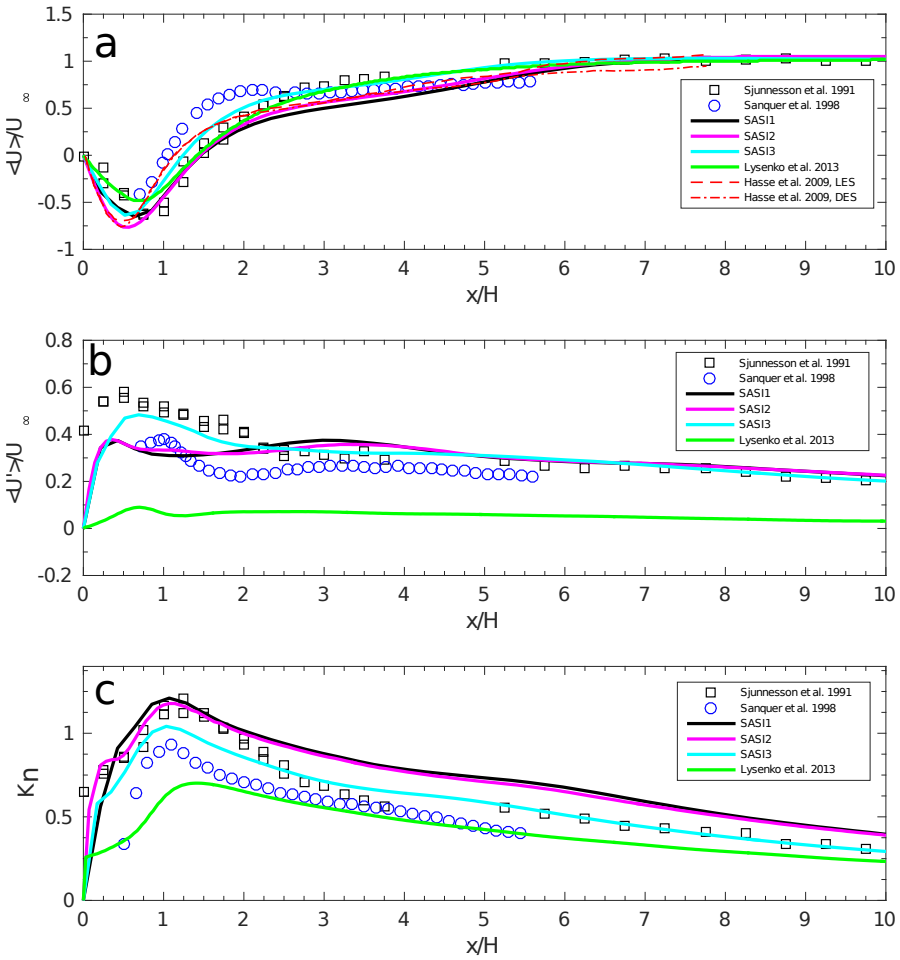

Fig. 4 Normalized mean stream-wise velocity (a), its fluctuations (b) and and normalized turbulence kinetic energy (c) in the wake centerline for the Volvo test rig

experimental and numerical results. Some discrepancies were observed between mean velocities inside the recirculation zone. These deviations can be affected by the earlier laminar-turbulence transition in the separating shear layers. A lack of statistical convergence can also be suggested. In the present SAS, the recirculation zone length was predicted as $< L_r > /H = 1.4$ for the SASI1 and SASI2 runs, which was in a fairly good agreement with experimental data of Sjunnesson et al. [59], $< L_r > /H = 1.35$. It is interesting that Hasse et al. [22] predicted the recirculation lengths of the LES and DES models very similar to the present SAS results, which deviated only about 11% from the measurement ($< L_r > /H = 1.18$).

Also, it is worth to notice that the experimental data by Sanquer et al. [54] have been obtained for the Reynolds number, $\mathrm{Re}_h \approx 6 \times 10^3$, where the h is the

bluff body height (case i3). Another important parameter in this experiment, the blockage ratio (the ratio between bluff-body to channel heights) was 0.33 as in the Volvo test rig. The fluctuations of the axial stream-wise velocity and the turbulence kinetic energy measured by Sanquer et al. [54] had the lowest values compared to the data obtained for the Volvo test rig due to the lowest Reynolds number. As a consequence, the recirculation zone length measured by Sanquer et al. [54] had the lowest value, $< L_r > /H \approx 1$.

Figure 5 shows the turbulent structures for this flow using the Q-criterion, ($Q = S^2 - \Omega^2 = 5 \times 10^4$, where S is the strain rate and Ω is the vorticity). The dynamics of the downstream flow behind the bluff-body was largely driven by the shear layer and wake processes alone. For this Reynolds number range (sub-critical flow regime, $1000 < \mathrm{Re} < 200000$), both absolute and convective instabilities are present – asymmetric vortex shedding (the Bénard/von Kármán instability) and Kelvin-Helmholtz instability of the separated shear layer [57]. Investigation of the shear-layer instability was out of scope of the present work. The vortex shedding instability was periodic and had a characteristic frequency of $f_{vs} = \mathrm{St}\, U_\infty / H$, where St is the Strouhal number. As a general observation for circular cylinders, the Strouhal number is independent of Reynolds number ($\mathrm{St} = 0.21$) in the post-shear-layer transition. The Strouhal numbers determined from the Fast Fourier transform of the sampled velocity (about 1.8×10^5 samples during 40 vortex-shedding periods) were $\mathrm{St} = 0.28$, 0.27 and 0.30 for the SASI1, SASI2 and SASI3 runs, respectively. Results obtained by URANS and reported previously [31] were $\mathrm{St} = 0.28$. This value was in reasonable agreement with the experimental data by Sjunnesson et al. [59] and Sanquer et al. [54], who measured $\mathrm{St} = 0.25$ and $\mathrm{St} = 0.26$, respectively. This corresponded with the LES data reported by Manickam et al. [40] ($\mathrm{St} = 0.28$) and the Detached-Eddy Simulation by Hasse et al. [22] ($\mathrm{St} = 0.28$) for the same Volvo configuration and identical conditions.

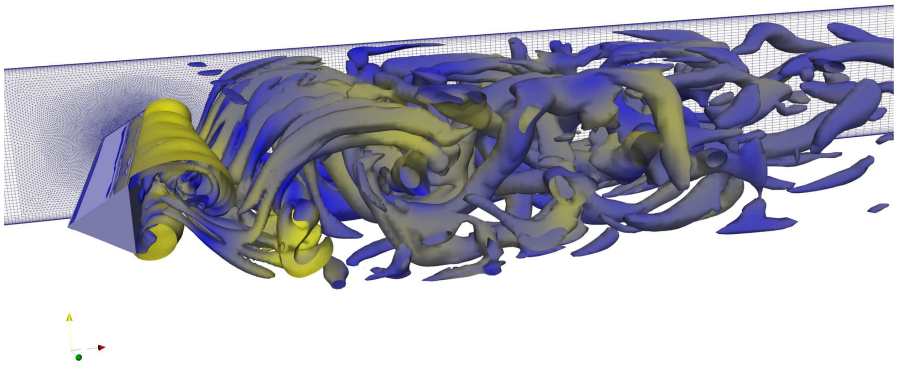

Fig. 5 Flow structures for the Volvo test rig. Iso-surface of the Q-criterion, $Q = 5 \times 10^4$

Figure 6 compares one-dimensional frequency spectra extracted from the present solutions at the downstream location $x/H = 1.75$ on the centerline of

the wake. About 1.8×10^5 samples of the cross-flow velocities were collected (or $N_{vp} \approx 35$). The spectra calculated from these time series were then averaged in the span-wise direction to increase the statistical meaning. To obtain the spectra, the Welch periodogram technique [66] was used. The frequency was nondimensionalized by the Strouhal shedding frequency (f_{vs}).

The spectra obtained by LES of Manickam et al. [40] and measured by Sanquer et al. [54] were added to compare the present SAS results with others numerical solutions. A $-5/3$ slope is shown as well. All numerical data sets yielded very similar power spectra. However, it is clearly seen that numerical solutions provided over-dissipative spectra in respect to the $-5/3$ slope. It is worth to notice that the present results were less dissipative than the LES data by Manickam et al. [40] and reproduced the same trend as the measured spectrum by Sanquer et al. [54].

It is well-known that the effect of an excessive dissipation of a numerical method led to a rapid decay of the spectrum so that no inertial subrange could be satisfactory captured. The over-dissipation of the present method could probably be explained by using the TVD scheme to approximate convective terms in the momentum equation, which is more dissipative compared to CDS-2 [8]. Additionally, the unstructured hexahedral/tetrahedral mesh was designed for the present calculations, which might have added extra dissipation to the method as well (impact of the sub-grid scale length was discussed briefly in Sec. 6.3). And, of course, the implemented procedure for the high frequency damping of the turbulent viscosity using the WALE sub-grid scale model can be considered.

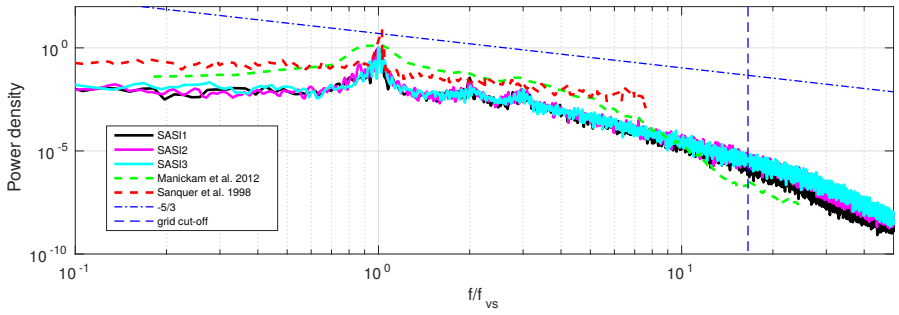

Fig. 6 One-dimensional spectra of the transverse velocity in the wake for the Volvo test rig: non reactive results

5.3 Combustion results for RANS/URANS

In this section some limited RANS/URANS results obtained using the EDC and TFC combustion models are presented. First, the effects of heat transfer was studied. For this purpose, several calculations with the conjugate (coupled fluid/solid interaction) heat transfer were carried out. Also, the influence

of the turbulence Schmidt number was investigated. Thereafter, the effects of the finite-rate chemistry were investigated using both global and detailed mechanisms. Finally, the model sensitivity to the operational conditions was provided. For sake of order, it is noted that the more general TFC implementation of Ansys Fluent (cf. Sec. 2.6) gave for all the present fully premixed cases a constant value for the mean mixture fraction and zero for its variance.

5.3.1 Heat transfer effects

Several RANS calculations were performed to investigate the influence of the heat transfer effects. For this purpose, the two-dimensional mesh was redesigned to calculate the conjugate (fluid/solid) heat transfer. A new computational zone was added to the mesh, which included the solid bluff-body. Fig. 7 displays contours of temperature. The combustion RANS was performed using the Ansys Fluent code. The premixed combustion was treated using the TFC model. The first run (RANS1) was calculated using the adiabatic conditions for all walls and excluded radiation. The second run (RANS2) included the conjugate and radiative (P1) heat transfer. The standard k-ϵ model was used for the turbulence closure for both cases. The third run (RANS3) was conducted to estimate the influence of the turbulence Schmidt number, which here was set to $\mathrm{Sc}_t = 0.4$. As it has been discussed in authors' previous studies [34]-[35], as well as in study by Yasari et al. [70], the values of $\mathrm{Sc}_t = 0.3 - 0.4$ compared to the more widely used values of $0.7 - 0.9$ can provide better agreement for several considered test cases. Afterwards, the temperature on the wall surfaces of the bluff-body was extracted and applied as the boundary conditions to the standard mesh in order to estimate the heat transfer effects for the EDC model (URANS5).

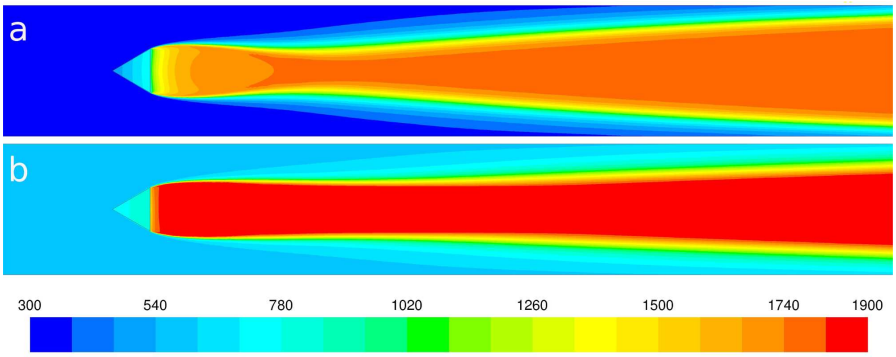

Fig. 7 Contours of mean temperature for the Volvo test rig for the case C1 (a) and the C2 (b), obtained by RANS2 and RANS4, respectively

Figure 8 displays comparison of the mean stream-wise velocity in several axial positions in the channel downstream of the bluff-body. In general, agreement between calculated and experimental results inside the recirculation zone

($x/H = 1.525$) was reasonable. The largest deviations were observed as occurring in the recovering region at $x/H = 3.75$ and $x/H = 9.4$, which could be explained by the fact that all runs significantly under-estimated the recirculation zone length. All runs (except RANS1) predicted approximately the same recirculation zone length of $L_r = 1.8$, which was significantly lower compared to the experimental value $L_{r,exp} = 3.55$. It is interesting that both EDC and TFC models provided qualitatively similar results. The difference between RANS1 and RANS2 is seen clearly as well. RANS1 provided more rapid flame brush expansion resulting in the shortest recirculation zone length.

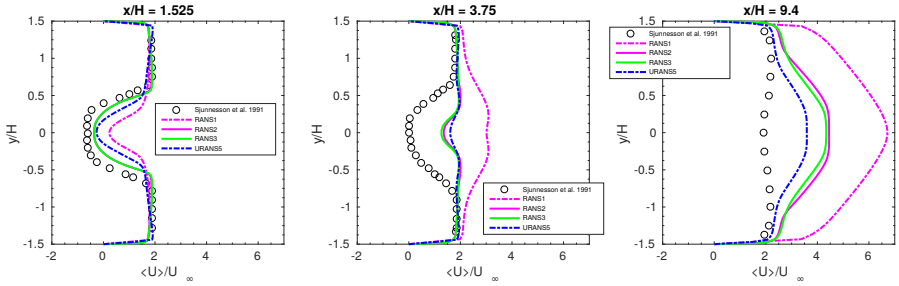

Fig. 8 Mean profiles of the normalized stream-wise velocity, obtained by RANS1, RANS2, RANS3 and URANS5 for the Volvo test rig

Figure 9 shows distributions of the mean mole fractions of $X_{\mathrm{CO_2}}$, $X_{\mathrm{O_2}}$ and temperature between the present and experimental results. The effects of heat transfer (RANS1 vs. RANS2) were a minimum at the axial stage $x/H = 3.75$ and increased significantly further downstream. The distributions of mean scalars had the same trends as the flame structure. The numerical results obtained by the EDC (URANS5) and TFC (RANS3) models agreed quite well between each other, in spite of small deviations for the mean temperature, where the EDC model slightly over-estimated the TFC results. Also, it is clearly seen that calculations obtained using the $\mathrm{Sc}_t = 0.4$ outmatched the results with $\mathrm{Sc}_t = 0.85$, which was consistent for the velocity fields as well.

5.3.2 Finite-rate chemistry effects

Several chemical kinetics schemes were chosen to investigate the finite-rate chemistry effects: global one-step and three-step as well as the full GRI-3.0 and San-Diego mechanisms as outlined in Sec. 2.5.2. Figure 10 compares the experimental data with the present results. In general, temperature profiles predicted by the EDC with different kinetics schemes matched the experimental data quite well. The EDC with all the kinetic schemes over-predicted the peak temperatures by about 150 K. However, this deviation can be explained by the simplified treatment of heat transfer effects near the solid walls (adiabatic conditions) and by the fact that the radiation losses were not taken into account. Insignificant deviations between all kinetics schemes were observed

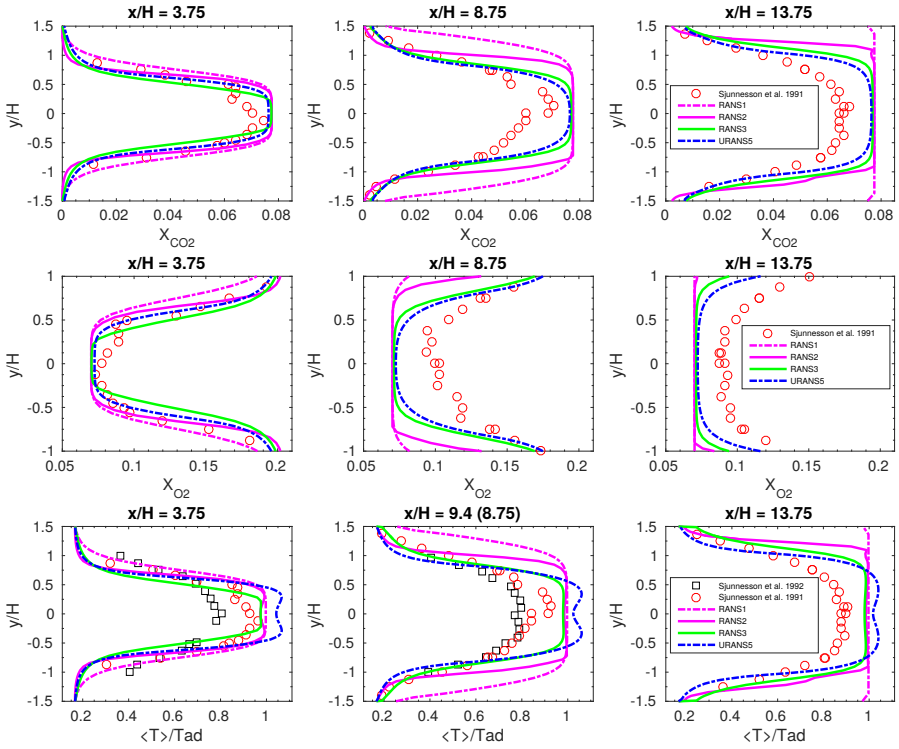

Fig. 9 Transverse profiles of mean mole fractions X_{CO_2}, X_{O_2} and temperature, obtained by RANS1, RANS2, RANS3 and URANS5 for the Volvo test rig

for the mole fraction of carbon dioxide as well as for the mole fraction of oxygen, O_2. It is interesting to note that GLB3 with the modified β in the third reaction provided damping of the temperature by $5-7\%$.

5.3.3 Effects of operational conditions

Several RANS and URANS calculations using both the TFC and EDC models were performed to investigate the models' sensitivity to the different operations conditions. For this purpose, the second baseline case (C2 from Table 2) from the series of experiments by Sjunnesson et al. [58],[59],[60] was chosen. It is worth noting that all present calculations were carried out for the equivalence ratio $\phi = 0.65$, while the CARS measurements have been obtained for the significantly lower value, $\phi = 0.58$. RANS4 and RANS5 were calculated using the TFC model and the same settings as RANS3 and RANS2. The only difference between RANS4 and RANS5 was for the value of the turbulence Schmidt number, $\mathrm{Sc}_t = 0.4$ and $\mathrm{Sc}_t = 0.85$, respectively. Fig. 7,b shows contours of the temperature obtained by RANS5. URANS6 and URANS7 were simulated using the EDC model with the different treatment of chemical kinetics, the global one-step reaction and the full San-Diego mechanism, respectively. The bound-

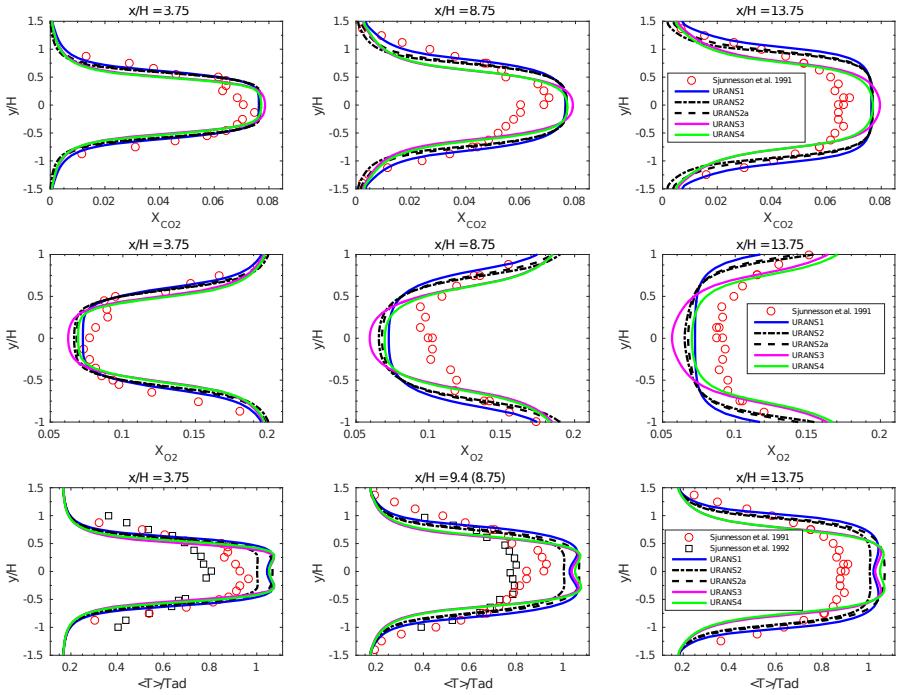

Fig. 10 Mean profiles of mean mole fractions X_{CO_2}, X_{O_2} and temperature for the Volvo test rig

ary conditions for the temperature on the bluff-body walls were interpolated from the data extracted from RANS5. The turbulence Schmidt number was set to $\mathrm{Sc}_t = 0.85$ for both URANS6 and URANS7, based on results obtained by the TFC model.

Figure 11 shows comparison of the mean molar fractions of X_{CO_2}, X_{O_2} and temperature at $x/H = 3.75$, 8.75 and 13.75 between the present and experimental results. At $x/H = 3.75$, satisfactory agreement was obtained between both experimental profiles and all four numerical runs with some small differences about of 5% and 10% for the peak temperatures and mole fractions, respectively. At $x/H = 8.75$, considerable deviations of about 20% were observed for the both mole fractions for all four runs. At the same location, the measured temperature was matched quite well by the EDC runs (URANS6 and URANS7), while the TFC runs (RANS4 and RANS5) provided satisfactory agreement with deviations of 10%. Further downstream, at $x/H = 13.75$, reasonable agreement (with deviations of about 10%) was observed for both mole fractions and temperature for all runs inside the flame. However, significant differences could be observed at the channel walls, where all numerical runs under-predicted the temperature (and mole fractions) at the channel walls. These discrepancies might be explained by the applied iso-thermal boundary conditions, which can be inaccurate for the flame-wall interaction.

The differences between RANS4 and RANS5 demonstrated the influence of the turbulence Schmidt number on the combustion process. The RANS4 run with $\mathrm{Sc}_t = 0.4$ gave a significantly narrowed profile of the temperature in the far wake (locations $x/H = 8.75$ and 13.75). In general, agreement between the global one-step reaction and the San-Diego mechanism obtained by the EDC runs was reasonable at locations $x/H = 3.75$, with the increased deviations further downstream at locations $x/H = 8.75$ and 13.75. This related to the expansion of the shear layers, where the burning occurs and the finite-rate chemistry effects are treated in different manners. Both EDC and TFC models predicted the peak mole fractions inside the flame with the same level of error. The predicted expansion of the flame thickness was considerably different between the EDC and TFC models as well.

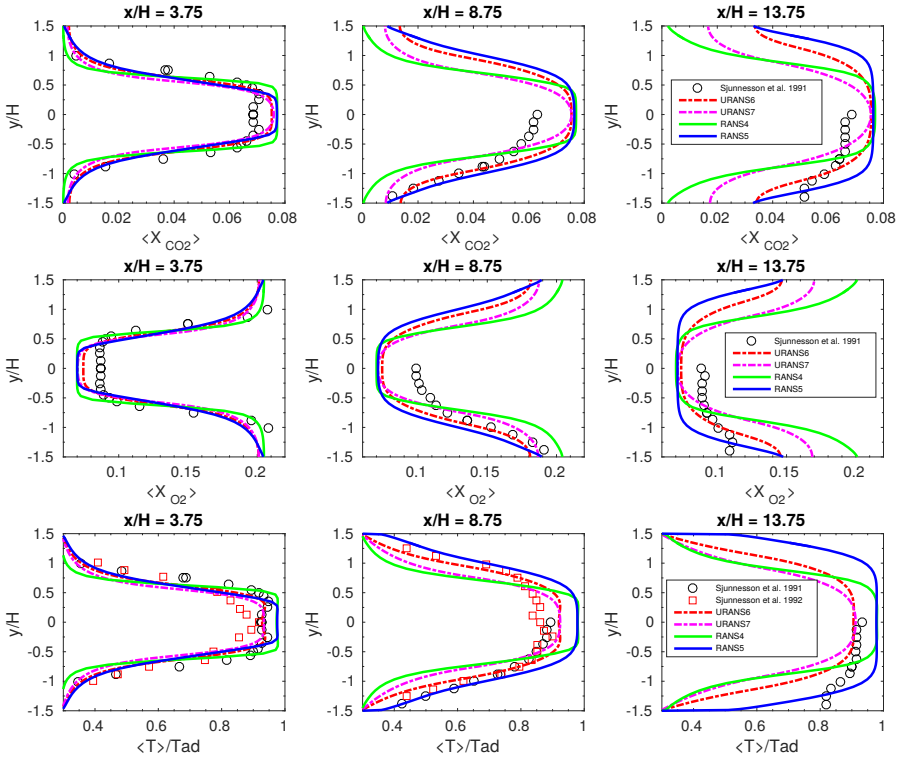

Fig. 11 Transverse profiles of scalar data obtained by RANS4, RANS5, URANS6 and URANS7 for the Volvo test rig

5.4 Combustion results for SAS and LES

The mean stream-wise velocity $< u >$ and the mean turbulence kinetic energy $< K_n >$ along the centerline are shown in Fig. 12. One can clearly see

that the LES results matched the experimental data by Sjunnesson et al. [59] with the reasonable agreement as well as the experimental data by Sanquer et al. [54] (Case r3). The differences between the Smagorinsky and the k-equation SGS models were insignificant. Some discrepancies can be observed in the vicinity of the bluff-body inside the recirculation zone, which could be explained be the simplified treatment of the heat transfer effects. The SAS results revealed significant under-prediction of the recirculation zone length, which could possibly be explained by, besides of the effects of heat transfer, the RANS treatment of the turbulence-chemistry interaction. Indeed, the SAS results for the mean stream and transverse velocities were quite similar to those provided by the RANS/URANS calculations (see, for example, Fig. 10). The axial distributions for $< K_n >$ had the same trends as the stream velocities. However, it is interesting to note that the Smagorinsky model (LESR2) provided significantly higher distributions of the turbulence kinetic energy. Such over-estimation could, possibly, be explained by setting of the Smagorinsky constant. Manickam et al. [40] and Ma et al. [36] have applied $C_s = 0.1$ in their reactive simulations of the Volvo rig. Furthermore, as it was discussed by Ma et al. [36], the Smagorinsky model is known to be sensitive to the level of heat release [11]. In the present study, to avoid excessive dissipation the Smagorinsky constant, $C_s = \left(c_k^3/c_\epsilon\right)^{1/4}$, was set to $C_s = 0.053$, which is slightly lower than the conventional minimum limit $C_s = 0.065$.

The mean recirculation zone lengths were predicted by SAS and LES as $< L_r > /H = 1.36 - 1.53$ and $< L_r > /H = 3.23 - 3.75$, respectively. The experimental values measured by Sjunnesson et al. [59] and Sanquer et al. [54] were $L_{r,exp}/H = 3.34$ and $L_{r,exp}/H = 2.88$, respectively.

Figure 13,a presents distribution of the normalized mean stream-wise velocity and its fluctuation in several axial positions in the channel downstream of the flame-holder. The agreement between the predicted and measured $< u >$ obtained by the LES models was reasonable, while the SAS results provided the largest deviations for the velocity field and recirculation zone length leading to the greater axial flow acceleration in the wake.

Inside the recirculation zone, LES models failed to reproduce the measured profile of the mean stream-wise velocity fluctuations. One of the possible explanations for these discrepancies could be insufficient grid resolution of the separated shear layers. Outside of the recirculation zone, reasonable agreement was observed for the k-equation SGS model, whereas the Smagorinsky model provided over-estimated values of $< u' >$ following Fig. 12,b. The SAS model predicted the mean stream-wise fluctuating velocity reasonably well inside the recirculation zone. Outside of the recirculation zone, significant under-estimation could be observed.

Instantaneous flame visualizations using the Q-criterion predicted by SAS and LES models are shown in Figs. 14-15. Both SAS and LES displayed symmetrical flame propagation or symmetrical vortex shedding, which was observed experimentally with high-speed video and Schlieren imaging [58]. As expected, the flow structures obtained by the LES runs contained larger

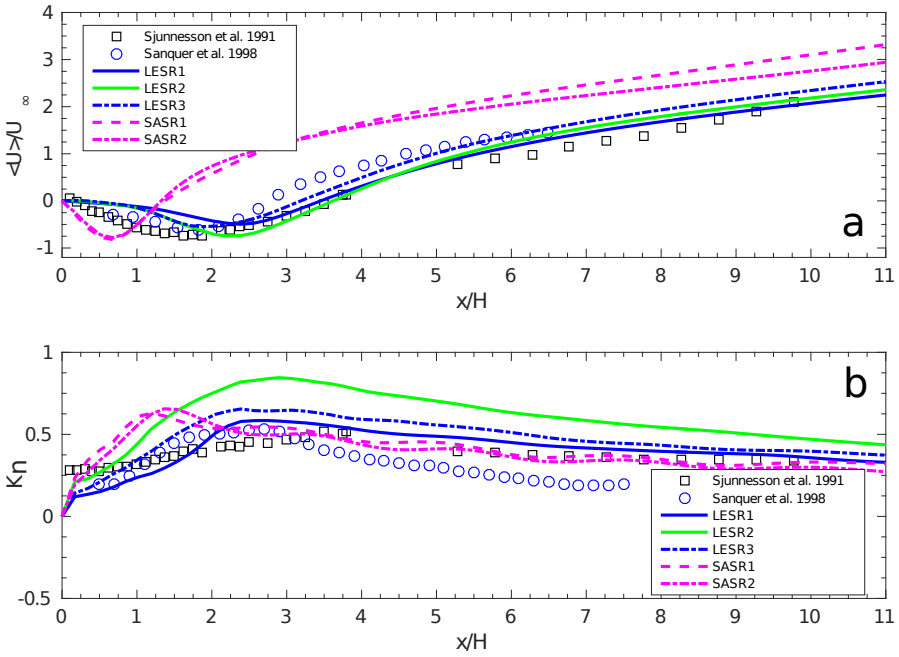

Fig. 12 Mean profiles of the normalized axial velocity (a) and the turbulence kinetic energy (b) obtained by the reactive SAS and LES models for the Volvo test rig

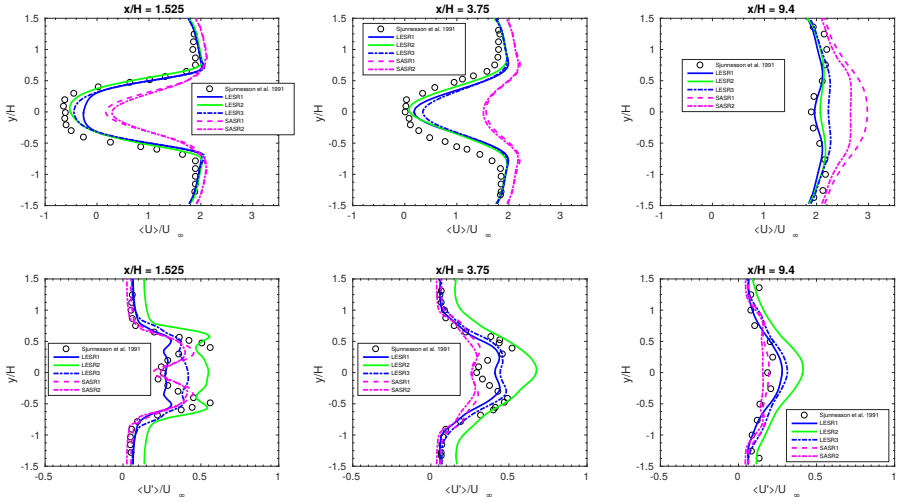

Fig. 13 Mean profiles of the normalized stream-wise velocity and its fluctuations obtained by the reactive SAS and LES models for the Volvo test rig

amounts of small-scale structures clearly corresponding to the difference between the SAS and LES approaches. Principle distinguish between LES and SAS approaches resulted in a wider and less wrinkled flame obtained by the SAS runs. Another interesting observation following from Fig. 15 is that the LESR2 run predicted a staggered pattern due to vortex-vortex and vortex-flame interactions.

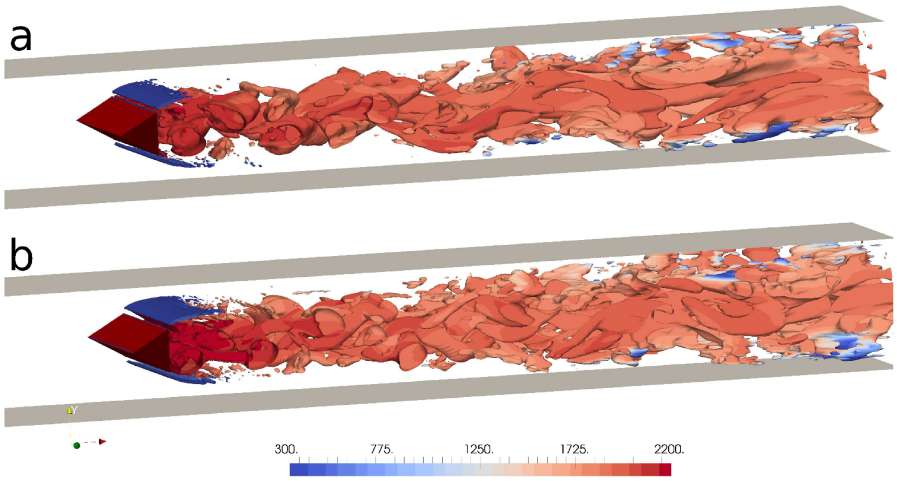

Fig. 14 Flow structures obtained by the reactive SASR1 (a) and SASR2 (b) for the Volvo test rig. Iso-surface of the Q-criterion ($Q = S^2 - \Omega^2 = 1 \times 10^4$, where S is the strain rate and Ω is the vorticity) colored according to the temperature [K]

The bluff-body combustion process is characterized by an existence of large vortex structures and their shedding in the near wake of the triangular cylinder, where the convective Kelvin-Helmholtz instabilities plays a dominating role. In the present study, the vortex shedding frequencies were predicted as $f_{vs} = 201$ Hz and $f_{vs} = 140 - 165$ Hz by SAS and LES models, respectively. Fig. 16 displays turbulent energy spectra extracted from the present LES and SAS solutions at the downstream location $x/H = 1.75$ on the centerline of the wake. The frequencies in Fig. 16 were normalized by the relevant vortex shedding frequency. For the sake of completeness, the reactive LES results by Manickam et al. [40] were added, in spite of the fact that these results were calculated for the C2 case, as well as the measured spectrum by Sanquer et al. [54]. The calculated spectra by LES and SAS models displayed a $-5/3$ region clearly. The spectra by all LES runs collapsed well with the measured spectrum by Sanquer et al. [54] and showed the similarity of the coherent structures in the reactive wake. It was clearly seen that the SAS results provided more dissipative spectra compared to the present LES runs. It is interesting that the spectra by SAS-EDC were quite similar to the spectra reported by Manickam et al. [40].

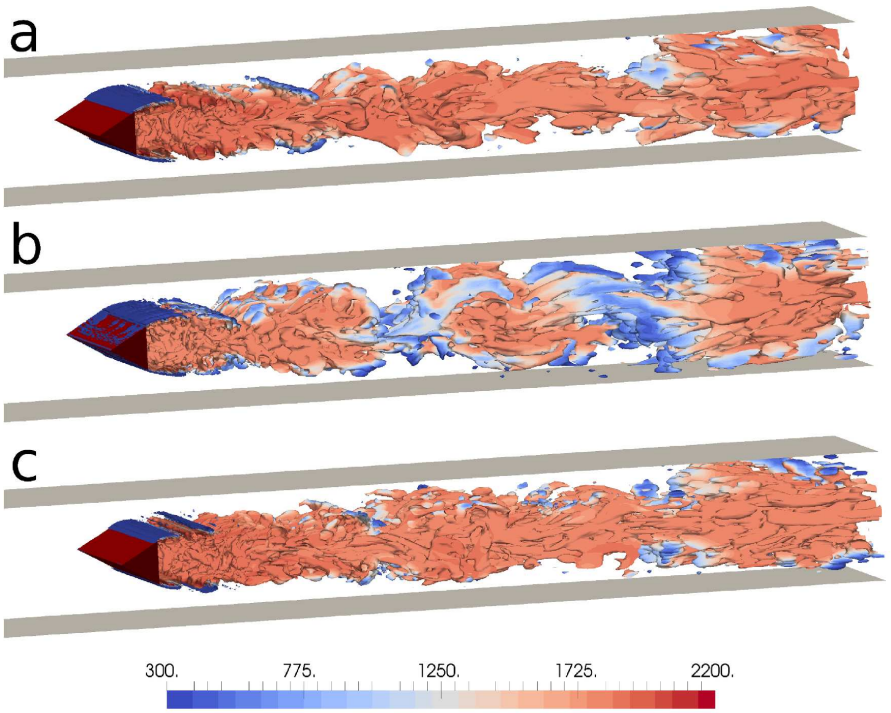

Fig. 15 Flow structures obtained by the reactive LESR1 (a), LESR2 (b) and LESR3 c) for the Volvo test rig. Iso-surface of the Q-criterion ($Q = S^2 - \Omega^2 = 1 \times 10^4$, where S is the strain rate and Ω is the vorticity) colored according to the temperature [K]

Like the Fourier transform, Fig. 16 provides the 1D continuous wavelet transform (CWT hereafter) for SASR1 and LESR1 and LESR2, where the small coherent structures of the flow are visualized. Here, CWT was based on the Morlet wavelet, which allows to determine efficiently the energy containing structures (coherent structures) in the flow signal [33], [35]. The details of CWT have been provided in one of the authors' previous studies [33]. It can be seen clearly, that for the SASR2 case most of the high-frequency coherent structures were fully overwhelmed by dissipation. Also, it was shown that SASR2 had more pronounced and regular vortex shedding compared to LESR1 and LESR3. Another observation following from Fig. 16 was that the nature of vortex shedding obtained by reactive LES appeared intermittent. Energy peaks did not always appear at the same frequency, and there was a broadband variation in the localized peaks along time.

Figure 17 compares both the CARS measurements [60] and the gas analysis data [58] with the numerically predicted results. Note the experimental data by CARS and gas analysis have been collected at different positions ($x/H = 9.4$ for CARS and $x/H = 8.75$ for gas analysis). It can be noted that the

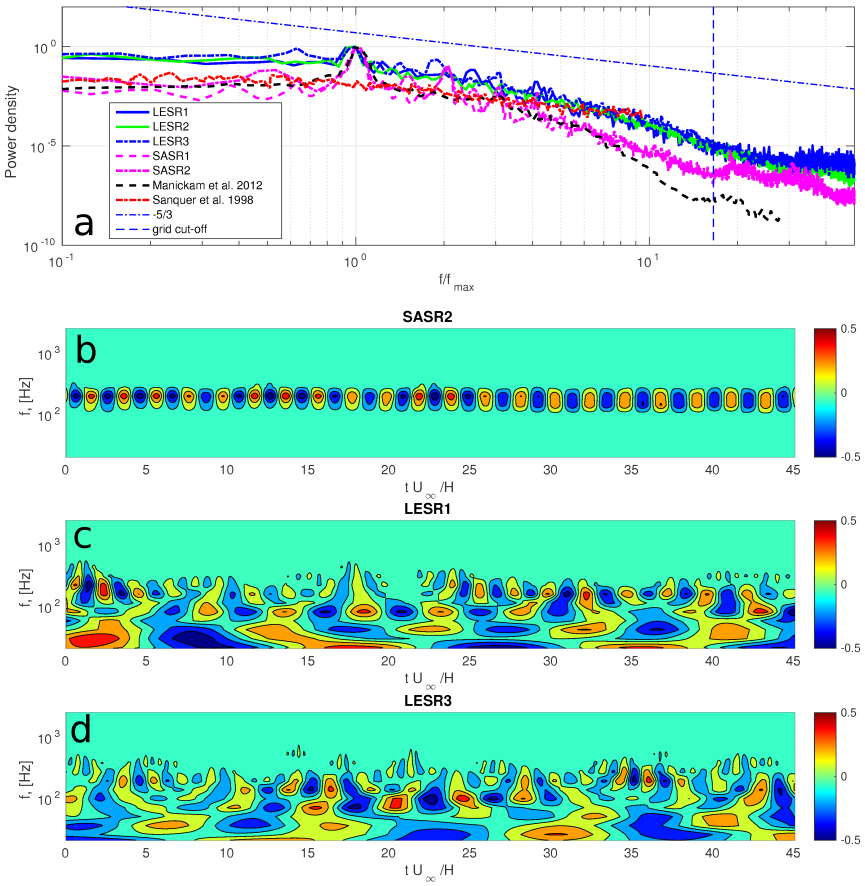

Fig. 16 Fourier power spectra (a) and wavelet coefficient energy (b-d) of the transverse velocity in the wake for the Volvo test rig: reactive SAS and LES results

temperature of the experiments was computed from the measured species, assuming equilibrium chemistry.

Both LES and SAS runs failed to predict temperature inside the recirculation zone (location $x/H = 0.95$), which could possibly be explained by the fact that heat transfer effects were not taken into account. Outside the recirculation zone, satisfactory agreement between LES and SAS runs was observed. The LESR2 run, with the Smagorinsky SGS model, provided the most accurate predictions, while the LESR1 and LESR3 runs, with the k-equation model, slightly over-estimated the temperature profiles. SAS results predicted more sharpened and over-estimated distribution of the mean temperature profiles (due to the wider and less wrinkled flame structure), compared to the experimental data as well as to the LES results. In terms of temperature fluctuations, LES models had quantitatively and qualitatively distributions similar to the experimental values. However, the Smagorinsky model had the trend to over-

estimate the pulsations in the flame core, while the k-equation model resulted in its under-estimation. The SAS results failed to reproduce the temperature fluctuations in the flame core even qualitatively.

Several transverse distributions of the mean mole fractions $X_{\mathrm{CO_2}}$ and $X_{\mathrm{O_2}}$ are shown in Fig. 18. Numerical results, obtained by both SAS and LES models and the corresponding trends as the temperature profiles related to the visualized flames.

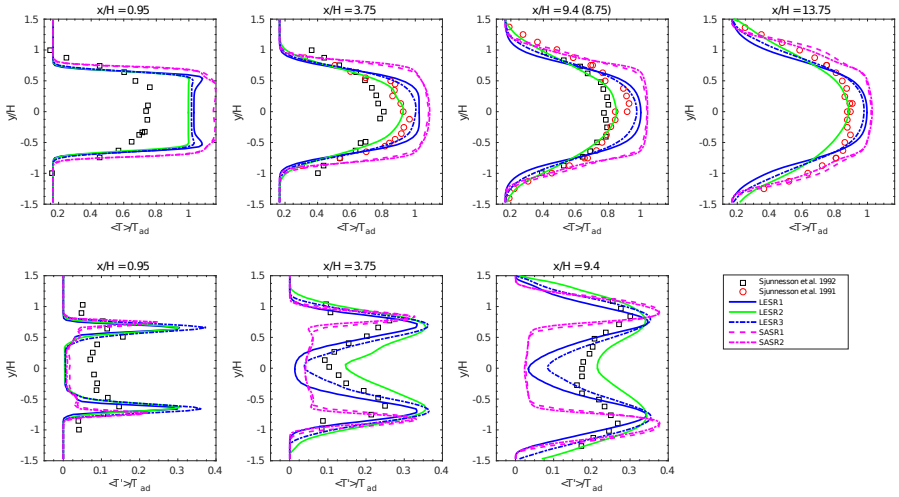

Fig. 17 Transverse profiles of normalized mean temperature and its fluctuations obtained by the reactive SAS and LES models for the Volvo test rig

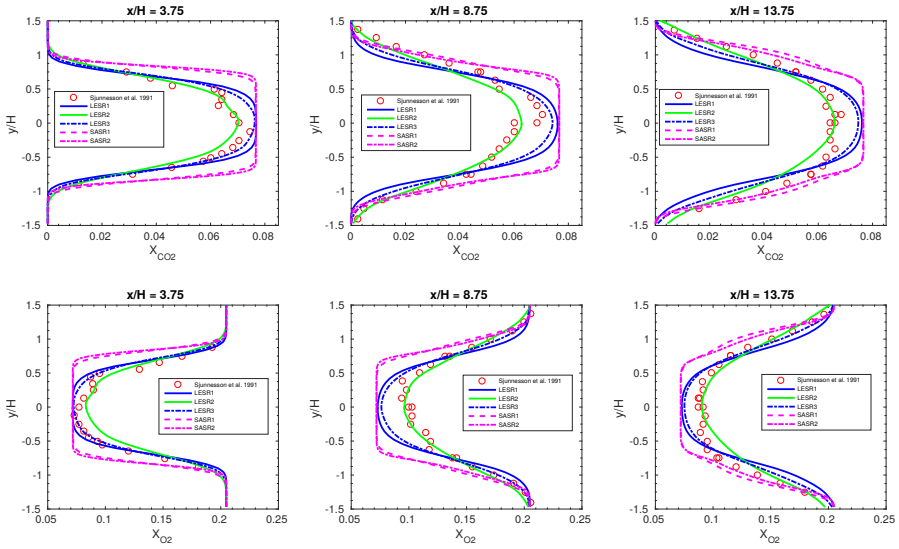

Fig. 18 Transverse profiles of the mole fractions X_{CO_2} and X_{O_2} obtained by the reactive SAS and LES models for the Volvo test rig

6 Discussion

Disagreements between experimental data and numerical results were determined by two groups of errors (apart from experimental errors): (1) model errors due to inadequate assumptions made in selecting one sub-model or another (for turbulence, radiation and turbulence-chemistry interaction) and (2) discretization errors caused by the inadequate resolution of the employed computational grids and computational methods.

It can be noted that all SAS and LES runs discussed in the present work have been calculated using the global one-step mechanism (GLB1).

6.1 Influence of modeling errors

From the modeling point of view, the following groups of physical processes related to the complex combustion phenomena have to be modeled: the turbulence, the chemistry, the turbulence-chemistry interaction and the heat and mass transfer.

6.1.1 Overview of capabilities to predict turbulent combustion by URANS, SAS and LES

Figure 19 displays the spatial profiles of the mean stream-wise velocity and the mean temperature at three different locations in the wake obtained by the different modeling approaches. All models have some kind of interrelation

and similarity in the estimation of the turbulence kinetic energy by using a separate transport equation, although the viscous dissipation is treated in a different manner.

The most accurate results to predict the recirculation zone length was obtained by the LES-EDC closure, while the SAS and URANS results significantly under-estimated L_r. This observation was made in spite of the fact that both URANS and SAS calculations showed very satisfactory agreement for the inert flow conditions.

The discrepancies between URANS, SAS and LES for the temperature and other scalar fields had the similar qualitative behavior. In general, the present LES-EDC closure provided superior results over the URANS and SAS models. Also, it can be seen clearly that URANS and SAS calculations yielded a sharper spatial distribution of the temperature compared to the parabolic-like shape predicted by LES-EDC. At the location $x/H = 0.95$, all three models yielded significant over-estimation of the flame temperature, mostly due to the simplified treatment of the heat and mass transfer effects. Further downstream, at the locations of $x/H = 3.75$ and 9.4, the temperature profiles obtained by URANS, SAS and LES had the similar qualitative behavior, nevertheless, URANS and SAS yielded sharper profiles with some over-estimation of the peak flame temperature. These can be possibly explained by the excessive viscous dissipation in the shear layers generated by URANS and SAS models, which consequently results in predictions of related time and length scales used in the EDC-PSR formalism to calculate reaction rates.

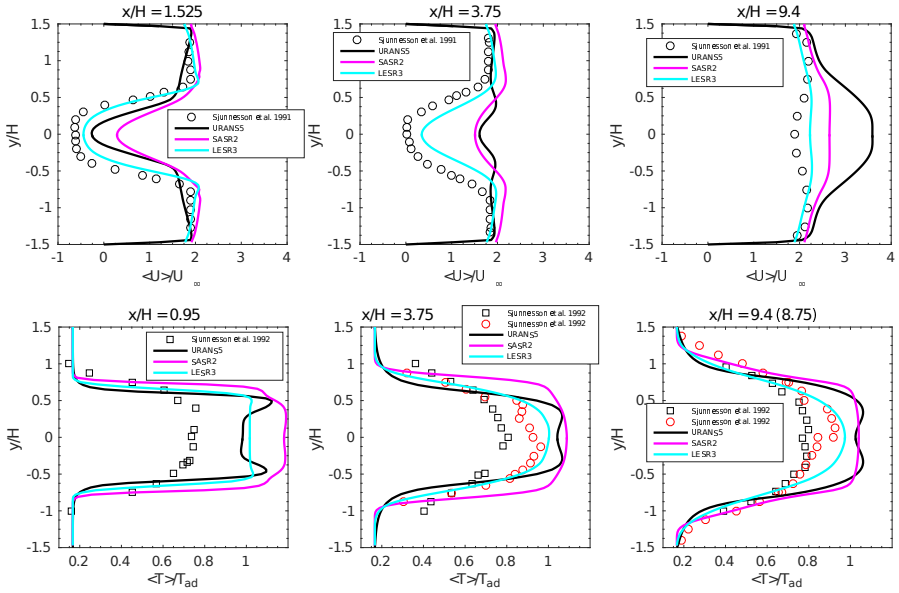

Fig. 19 Normalized mean stream-wise velocities and temperatures predicted by different modeling approaches: URANS5, SASR2 and LESR3

6.1.2 Effects of heat and mass transfer

In the present study several RANS/URANS calculations were performed using the EDC and TFC closures with different values of the turbulence Schmidt number. It was observed that for the flow conditions C1 ($T_\infty = 300$ K), $\mathrm{Sc}_t = 0.4$ provided superior results compared to its conventional value of $\mathrm{Sc}_t = 0.85$. This finding was consistent with authors' previous results [34], [35], as well as other data available in the literature [55], [70], and valid for both the EDC and TFC closures. Further analysis of the numerical results for the C2 operational conditions ($T_\infty = 600$ K) showed that calculations with $\mathrm{Sc}_t = 0.85$ yielded slightly better agreement with the experimental data than the similar runs with $\mathrm{Sc}_t = 0.4$. However, this observation was valid only in the far wake (at $x/H = 0.8$ and further downstream), where the strong interaction between the flame and the channel walls occurred. In the near wake (and inside the recirculation zone), noticeable discrepancies between $\mathrm{Sc}_t = 0.85$ and $\mathrm{Sc}_t = 0.4$ were not found.

The effects of heat losses in the vicinity of the bluff body were investigated using several RANS calculations and the TFC closure. Fig. 20 displays the spatial mean temperature profiles for different operational conditions in the vicinity of the flame holder at the location $x/H = 0.95$. It can be observed that the heat losses gave a damping of about $5\% - 8\%$ in the temperature in the vicinity of the bluff-body. However, further downstream at the location of $x/H = 3.75$, the effects of heat losses were mostly vanished. The remaining discrepancies between the RANS calculations and the CARS measurements can be explained by the slightly different fuel-to-air ratios used in the simulations ($\phi = 0.65$) and experiments ($\phi = 0.58 - 0.61$).

Figure 21 presents the effect of heat losses on development of the velocity field and the prime recirculation zone just downstream of the bluff-body. Here, limiting cases with the adiabatic (RANS7 and RANS6) and fully-CHT (RANS3 and RANS5) boundary conditions were compared for the both flow conditions C1 and C2, respectively. It can be observed that the length of recirculation zone was significantly increased when the heat transfer effects were taken into account for both operational conditions. Thus, the recirculation zone increased from $< L_{r,ad} > /H = 1.492$ to $< L_r > /H = 2.5$ for the flow conditions C1 ($< L_{r,exp} > /H = 3.55$), and from $< L_{r,ad} > /H = 2.25$ to $< L_r > /H = 3.58$ for the flow conditions C2 ($< L_{r,exp} > /H = 3.16$), respectively.

6.1.3 Effects of the turbulence-chemistry interaction

Recent numerical results by Jones et al. [26] were used to assess the influence of the turbulence-chemistry interaction models for the reacting LES. Jones et al. [26] studied the Volvo test rig using LES and a sub-grid scale probability density function (LES-PDF, hereafter) approach in conjunction with the stochastic fields solution method to account for the subgrid scale turbulence–chemistry interactions. Numerical results by Ma et al. [36] were added

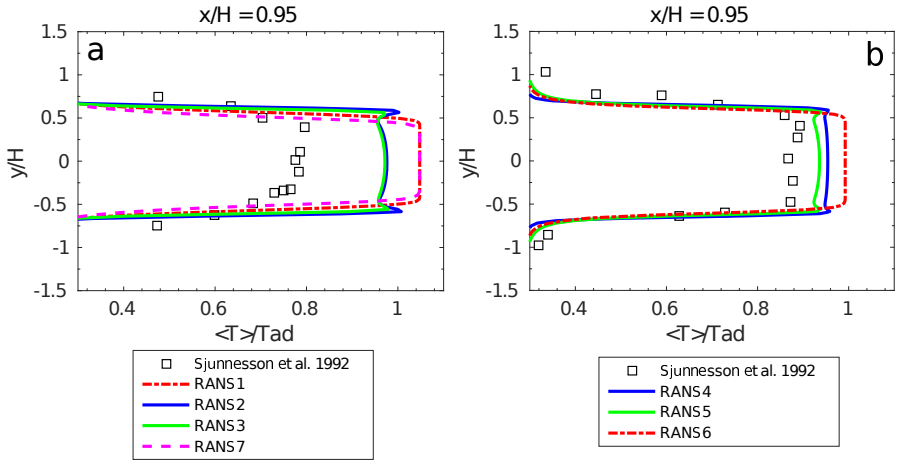

Fig. 20 Effects of heat losses depending on the operational conditions C1 (a) and C2 (b) for the Volvo test rig

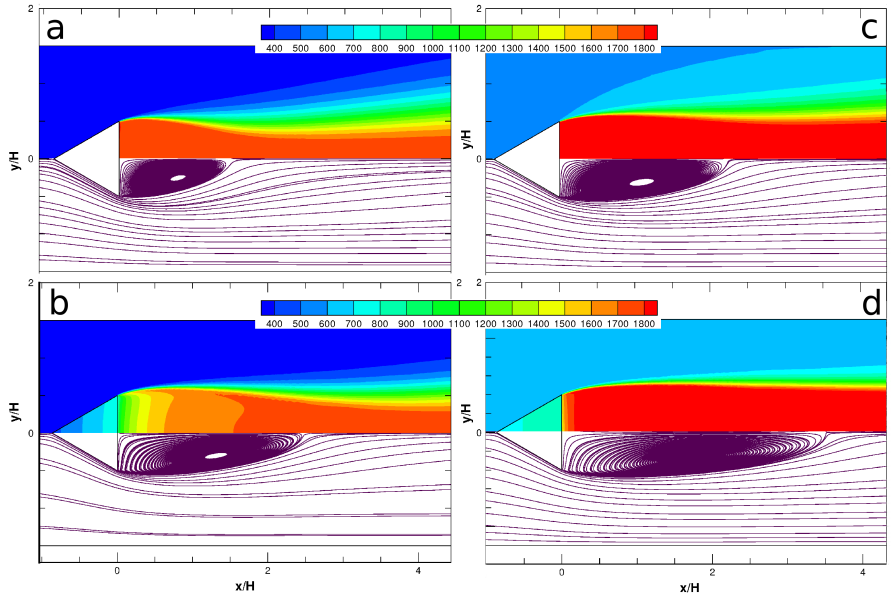

Fig. 21 Effects of heat losses on the velocity field depending on operational conditions C1 (a – RANS7, b – RANS3) and C2 (c – RANS6, d – RANS5) for the Volvo test rig

in spite of the fact that these results have been calculated for the C2 flow conditions ($T_\infty = 600$ K, $\phi = 0.58$).

Ma et al. [36] developed a reaction rate closure derived from the scalar dissipation rate (LES-SDR, hereafter), which has been assessed based on simultaneous a priori DNS analysis and a posteriori LES analyses. The LES-EDC

results (LESR2) based on the conventional Smagorinsky model were chosen for comparison.

Figure 23 displays profiles of the mean temperature and its fluctuation. At location $x/H = 0.95$, LESR2 provided the more sharpened, cone-like mean temperature profile, which over-predicted the measurements. The fluctuations of the temperature obtained by LESR2 were also more sharpened in the regions where mixing of fresh reactants and burnt products and combustion took place. Outside the recirculation zone, at locations $x/H = 3.75$ and $x/H = 9.4$, LESR2 yielded approximately the same qualitative and quantitative results for the mean temperature. For the temperature fluctuations LESR2 provided the same qualitative trends.

It is worth noticing that Jones et al. [26] and Ma et al. [36] used the conventional Smagorinsky SGS model with $C_s = 0.1$ for the turbulence closure. Here, the additional LES run (LESR4) using the Smagorinsky SGS model ($C_s = 0.1$) was calculated to investigate the influence of C_s. Fig. 23 shows that the discrepancies between LESR2 and LESR4 were minor for the mean temperatures, while the LES results with $C_s = 0.1$ revealed significantly worse predictions of the temperature fluctuations. On the one hand, one of the possible explanation for such behavior could be insufficient grid resolution. On the other hand, it might be explained by the fact that increasing the turbulence production leads to generation of large-scale vortex structures and their shedding in the turbulent wake and decreasing of the amount of small-scale structures.

The conventional Smagorinsky and the k-equation SGS models were tested for the inert and reactive LES. The present results did not reveal significant discrepancies between the Smagorinsky and the k-equation SGS models (Appendix B). For the reactive LES it was observed that the Smagorinsky model provided slightly better results compared to the k-equation SGS model. However, it is worth noting that the flame dynamics revealed by the Smagorinsky model was completely different with intermittency between pockets of fresh and burnt gases, which was probably not observed in the experiment. So it is important to stress that a change in the predicted behavior of the flame dynamics can be brought about by a change of the SGS model. It seems that the low Smagorinsky model constant is required for making the combustion model work correctly, as the model constant hardly affected the results obtained without combustion (Appendix B).

Manickam et al. [40] have discussed that the baroclinic vorticity could be one of possible reasons to explain such behavior of the Smagorinsky model. They showed that the baroclinic generation of vorticity occurred due to draining of heavy fresh mixture downwards and light hot gas moving upwards in the recirculation region due to the difference in pressure. Figure 22 compares the flow structures colored by the baroclinic contribution ($\rho^{-2}\nabla\rho\times\nabla p$), obtained for the reactive LES using the Smagorinsky and the k-equation SGS models. Figure 22 displays that the effects by the baroclinic contribution were more pronounced for the Smagorinsky model. These findings are strongly prelimi-

nary, and other factors like the volumetric expansion and self-diffusion due to the effective molecular viscosity [5] should be considered as well.

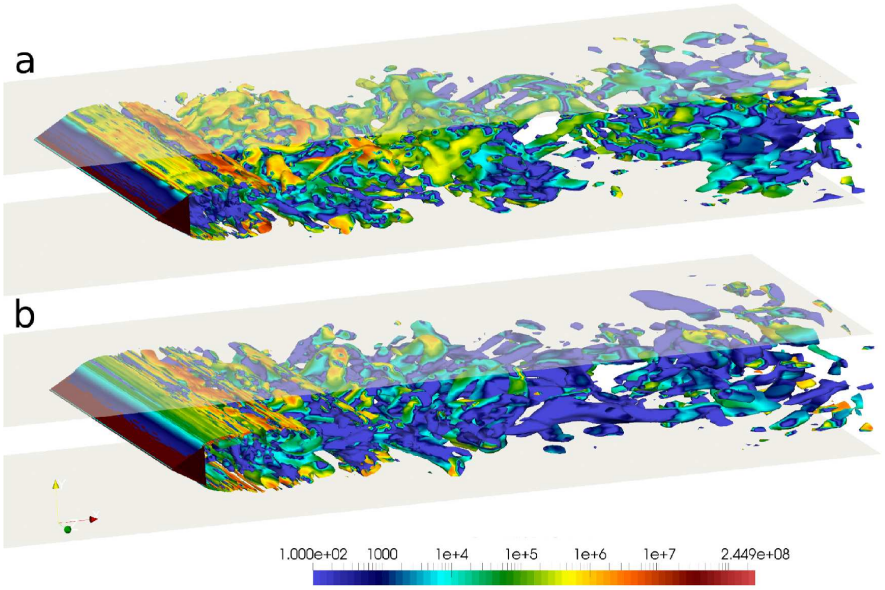

Fig. 22 Flow structures obtained by the reactive LESR2 (a) and LESR1 b) for the Volvo test rig. Iso-surface of the Q-criterion colored according to the magnitude of baroclinic contribution, $\rho^{-2}\nabla\rho \times \nabla p$

Comparison of the present predictions obtained by the LES-EDC closure with experimental data (and the LES-SDR and LES-PDF models) in terms of first- and second-order statistics, temperature and other scalar data, as well as energy spectra and wake dynamics, showed that the LES-EDC closure gave surprisingly similar results and very good agreement with experimental data. Moreover, this finding was in accordance with the results provided by Baudoin et al. [5], who investigated different finite-rate chemistry LES closures for the Volvo test rig and achieved satisfactory agreement with experimental data as well.

One of the possible ways to explain the reason for such good agreement can be described as follows. Turbulent combustion physics in a very simple manner can be characterized by the three governing mechanisms: the growth of flame brush thickness, evaluation of the turbulence diffusion and the development of the turbulent flame speed (burning velocity) [55]. The growth of the flame brush thickness is controlled by the large-scale turbulent eddies and accompanied by a slow growth of the turbulent flame speed, which is mainly controlled by the small-scale eddies [55]. For the LES-EDC closure the turbulence diffusion was approximated by the commonly used gradient model. Mixing and reactions are assumed to take place in the fine structures, sur-

rounded by large-scale flow structures. At the same time, the growth of the flame thickness is controlled by the resolved large-scale eddies. Under certain assumptions it is possible to calculate the turbulence flame speed and the turbulence flame thickness using the sub-grid residence time and the reactive volume fraction, γ^*, from the LES-EDC closure as $S_t = S_L\sqrt{\gamma^*\left(1 + D_k/D\right)}$ and $\delta_t = \delta_l\sqrt{\left(1 + D_k/D\right)/\gamma^*}$, where δ_l is the laminar flame thickness [5].

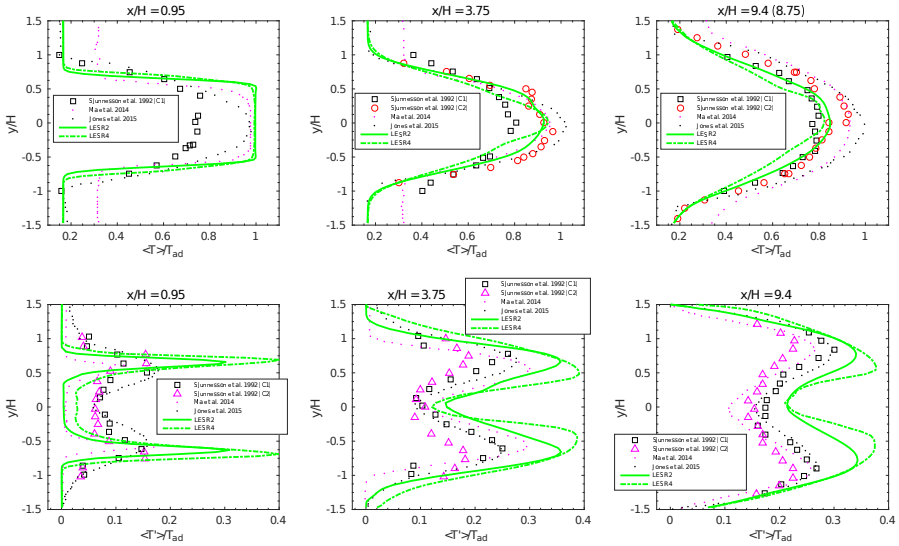

Fig. 23 Normalized mean and fluctuating temperatures predicted by the LES-EDC (LESR2 and LESR4), LES-SDR (Ma et al. [36]), LES-PDF ([26]) and experimental data for the Volvo test rig. Experimental data relevant to the LES-SDR (C2) are added for consistency

6.2 Effects of the sub-grid scalar flux modeling

The gradient hypothesis model (GHM) was used for the sub-grid flux closure in the present study. It worth noting that recent findings [1], [28], [36] showed that the accurate modeling of the sub-grid flux (SGSF) can be important and the interaction of chemical source term and the sub-grid flux modeling is of considerable importance for LES and should not be ignored. Klein et al. [28] investigated several SGSF models and demonstrated that the gradient hypothesis model was not very successful in representing the SGSF term obtained by DNS, but provided satisfactory performance in combination of a recently proposed the filtered value of combined reaction rate and molecular diffusion rate closure.

Here, we performed calculations of the SGSF effects on both inert and reactive flows, where GHM was replaced by the approach proposed by Clark et al. [10]. Preliminary results are provided in Appendix C. The present findings

did not reveal any significant deviations between GHM and the Clark tensor diffusivity model both for the inert and reactive simulations.

It is interesting to note that the present results were consistent with data reported by Allauddin et al. [1], who investigated the possible interaction of the SGSF term and numerical truncation errors. It is important to highlight that Allauddin et al. [1] used the OpenFOAM code with the TVD schemes for the reactive LES. They showed that the numerical error and the SGSF term had the same order of magnitude and qualitatively similar behavior for the considered cases, meaning that an explicit SGSF model might have a reduced or even disadvantageous effect.

6.3 Influence of discretization errors

From the discretization error point of view, the spatial and temporal discretization errors can be considered. Usually the spatial discretization error effects are larger than the error arising from the time integration [17]. It can be shown that in case of fully developed turbulent flows, existing small time and space scales are simply advected by the most energetic eddies [17]. This argument yields an accuracy time-scale similar to the Courant-Friedrichs-Lewy (CFL) criterion. Thus, in all present calculations, the stability condition CFL < 0.75 was employed, which guaranteed that the actual time step was close to the accuracy time step.

Several calculations were performed to investigate the spatial discretization error on the present SAS and LES results. It was interesting to see that the non-reactive SAS results obtained on the refined mesh, provided some improvement in the accuracy of the mean flow field, both for the first and second order statistics, while at the same time keeping the similarity in the flow dynamics (energy spectra and vortex shedding). Simultaneously, the reactive SAS calculations did not show any significant enhancements in the predictions for the mean flow field as well as the wake dynamics. The results obtained by the combustion LES on the two grids showed some improvement in the accuracy for the second order statistics, while the first order statistics and wake dynamics were captured approximately with the same level of precision.

Finally, satisfactory agreement was obtained between the measured and resolved turbulence kinetic energy by the present SAS and LES (Figs. 4,c and 12,b), which can indicate, at least qualitatively, on the adequate spatial resolution of the used grids.

7 Concluding remarks

The prime goal of this work was the further development and enhancement of the EDC for predictive combustion simulations of high Reynolds number flows of practical interest using Large-Eddy Simulations. In the present study several enhancements of the core numerical method have been introduced, and

validation was extended to the lean premixed bluff-body combustion flame (the Volvo test rig).

The new ODE integrator LSODA was implemented to overcome rare difficulties related with the RADAU5 solver for solving global reactions. Several strategies to estimate the PSR's residence time were discussed and the most computationally efficient was suggested for further usage. The compressible formulation of the Scale-Adaptive simulation was implemented and integrated with the EDC closure. The validation of SAS against the inert measurements for the Volvo test rig showed quite good agreement between them. Both reactive LES and SAS were carried out to simulate the Volvo test rig. The conventional Smagorinsky and the k-equation SGS models were tested for the reactive LES. It was observed that the LES-EDC with the Smagorinsky model provided slightly better results compared to the k-equation SGS model. However, it is worth noting that the flame dynamics revealed by the Smagorinsky model was completely different with intermittency between pockets of fresh and burnt gases that was probably not observed in the experiment. The effects of the Smagorinsky constant were investigated as well and showed that LES-EDC results with $C_s = 0.053$ provided slightly more precise results compared to $C_s = 0.1$.

Additionally, the results obtained by the conventional RANS/URANS using the EDC and TFC closures were discussed, and various effects like the thermal losses, the different operational conditions and the finite-rate chemical kinetics were assessed. The RANS calculations with the conjugate fluid-solid heat transfer allowed to assess the thermal losses in the vicinity of obstacle and estimate its influence on temperature (about 7%). Impact of the turbulence Schmidt number ($\mathrm{Sc}_t = 0.4$ and 0.85) on heat and mass transfer showed that $\mathrm{Sc}_t = 0.4$ provided superior results over the more widely used numbers like $\mathrm{Sc}_t = 0.7 - 0.9$ for the C1 test conditions ($T_\infty = 300$ K), while noticeable discrepancies were not found for the C2 conditions ($T_\infty = 600$ K). Effects of the finite-rate chemistry were assessed by using four different kinetics schemes, including the full GRI-3.0 and San-Diego mechanisms and the one-step and three-step global reactions. In general, all kinetics schemes showed similar results for the scalar data (X_{CO_2}, X_{O_2}) and temperature, except of the three-step reaction, which revealed unphysical results for the burn-out of O_2.

The global descriptions of LES, SAS and RANS/URANS indicated a clear interrelation between these three approaches to simulation of the turbulent (combustion) flows [17]. In general, reasonable consistency for these different approaches was found in the present study as well as satisfactory agreement between the present simulations and measurements. The most accurate results were obtained using the large-eddy simulations, which revealed that the LES-EDC closure is capable to reproduce with satisfactory agreement the unsteady combustion physics of the lean premixed bluff-body flame specific to the Volvo test rig both qualitatively and quantitatively, and were reasonably comparable with some others results available in the literature [5], [26], [36] as well.

Overall, the present results give a reasonable indication on the adequacy and accuracy of the core numerical method and its readiness for further combustion application development.

Acknowledgements We are grateful to the Norwegian Meta center for Computational Science (NOTUR) for providing the uninterrupted HPC computational resources and useful technical support. Comments and recommendations for three anonymous and very skilled reviewers of the Journal have increased considerably the quality of the paper.

Compliance with ethical standards

– Funding: Except for the computer allowance acknowledged above, this study has not received any funding.
– Conflict of interest: The authors declare that they have no conflict of interest.

A General validation of the LSODA and RADAU5 ODEs solvers

Here, the validation and verification of the RADAU5 [20] and LSODA [48] integrators are provided. Three well-known non-stiff and stiff test problems were chosen for this purpose. The first test is a simple model of flame propagation, which has been introduced in the Matlab ODE suite [46], [56]. The second benchmark is the Van der Pol equation. The third test is the Robertson problem, which consists of a stiff system of three non-linear ODEs for chemical kinetics proposed by Robertson [50]. For sake of completeness, the validation has been provided for both implemented ODE integrators as well as against the state-of-the-art ODE suite available in Matlab [56].

All test cases have been computed with the same absolute and relative error tolerances equal to 10^{-8}.

A.1 One dimensional flame propagation

A mathematical model of one-dimensional flame propagation [46] can be described as

$$\frac{dy}{dt} = y^2 - y^3, \;\; y(0) = \delta, \;\; \left[0 < t < \frac{2}{\delta}\right], \tag{49}$$

where y represents the radius of the sphere, t is time and terms y^2 and y^3 come from the surface area and the volume. After igniting, the sphere grows rapidly until it reaches a critical size. Then, the radius of sphere stays at the same size because the amount of oxygen being consumed while combustion in the interior of the sphere balances the amount available through the surface. In this case the critical parameter is the initial radius δ, which determines the stiffness of the problem. A solution becomes stiff near $y(t) = 1$, increasing or decreasing rapidly toward that solution for small values of δ.

Figure 24 presents the results of integration of this problem for $\delta = 0.01$ and $\delta = 0.0001$. As can be seen, the deviations between all integrators were negligible. All codes computed the problem for both initial conditions.

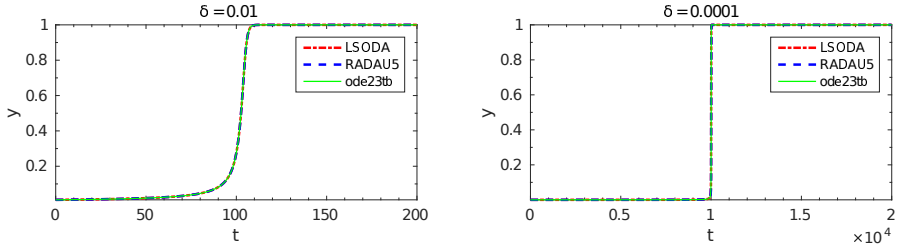

Fig. 24 Computed solution of the flame propagation problem obtained by RADAU5, LSODA and ode23td (Matlab) solvers

A.2 Van der Pol equation

The van der Pol equation is a second order ODE:

$$\frac{d^2 y_1}{dt^2} - \mu \left(1 - y_1^2\right) \frac{dy_1}{dt} + y_1 = 0, \tag{50}$$

where $\mu > 0$ is a scalar parameter.

The system of first-order equations can be obtained by making the substitution $dy_1/dt = y_2$:

$$\begin{bmatrix} dy_1/dt \\ dy_2/dt \end{bmatrix} = \begin{bmatrix} y_2 \\ \mu \left(1 - y_1^2\right) y_2 - y_1 \end{bmatrix}, \quad \begin{bmatrix} y_1(0) = 2 \\ y_2(0) = 0 \end{bmatrix}, \tag{51}$$

The nonstiff system ($\mu = 1$) was computed on the time interval [0 20], while the stiff system ($\mu = 1000$) was calculated on the time interval [0 3000]. Figure 25 displays the computed solutions obtained by RADAU5, LSODA and Matlab. All three solutions collapsed well to each other without any significant deviations.

A.3 Robertson problem

This problem deals with a system of ODEs that describes the kinetics of an auto-catalytic reaction [50]. The structure of the reactions is

$$\begin{aligned} \mathrm{A} &\xrightarrow{k_1} \mathrm{B} \\ \mathrm{B} + \mathrm{B} &\xrightarrow{k_2} \mathrm{B} + \mathrm{C} \\ \mathrm{B} + \mathrm{C} &\xrightarrow{k_3} \mathrm{A} + \mathrm{C}. \end{aligned} \tag{52}$$

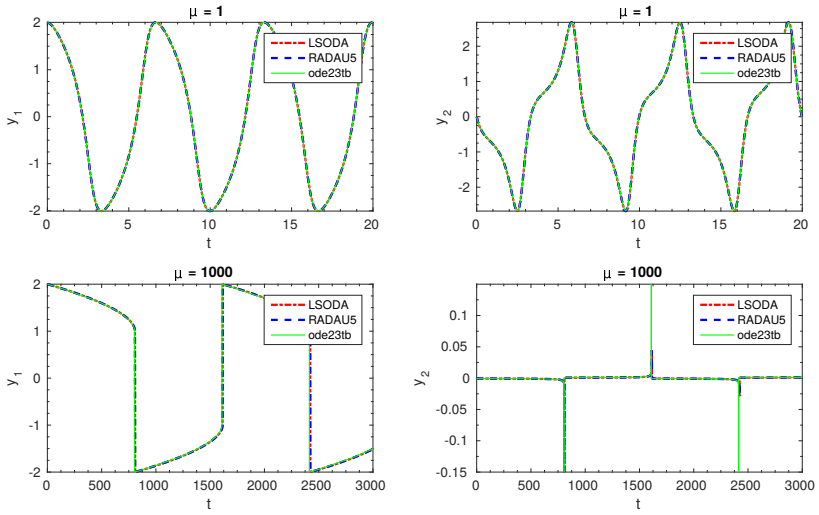

Fig. 25 Computed solutions of the nonstiff ($\mu = 1$) and stiff ($\mu = 1000$) van der Pol equation by RADAU5, LSODA and ode23tb (Matlab) solvers

Under some idealized assumptions [18], the following mathematical model can be set up as a set of three ODEs

$$\begin{bmatrix} dy_1/dt \\ dy_2/dt \\ dy_3/dt \end{bmatrix} = \begin{bmatrix} -k_1 \cdot y_1 & & k_3 \cdot y_2 \cdot y_3 \\ k_1 \cdot y_1 & -k_2 \cdot y_2^2 & -k_3 \cdot y_2 \cdot y_3 \\ & k_2 \cdot y_2^2 & \end{bmatrix}, \quad \begin{bmatrix} y_1(0) = 1 \\ y_2(0) = 0 \\ y_3(0) = 0 \end{bmatrix}, \tag{53}$$

where y_1, y_2, y_3 are the concentrations of species A,B,C respectively. The numerical values of the rate constants were $k_1 = 0.04$, $k_2 = 3 \times 10^7$ and $k_3 = 10^4$. The large differences among the reaction rate constants provide the reason for stiffness. Originally the problem was proposed on the time interval $0 < t \leq 40$, but it is convenient to extend the integration of solution on much longer intervals due to that many codes fail if t becomes very large.

Figure 26 presents the solutions obtained by RADAU5, LSODA and Matlab. Overall, the discrepancies between calculated solutions were negligible for y_1 and y_3. Small deviations between RADAU5, LSODA and Matlab integrators can be observed for y_2, which probably could be explained by the fact that Matlab has solved the rewritten system of differential algebraic equations by using the conservation law in order to determine the state of y_3, meanwhile RADAU5 and LSODA calculated the original system of equations.

B Effects of sub-grid scaling modeling on the inert flow for the Volvo test rig

Three non-reacting LES runs have been carried out to investigate the effects of the SGS models. For this purpose the k-equation and the Smagorinsky

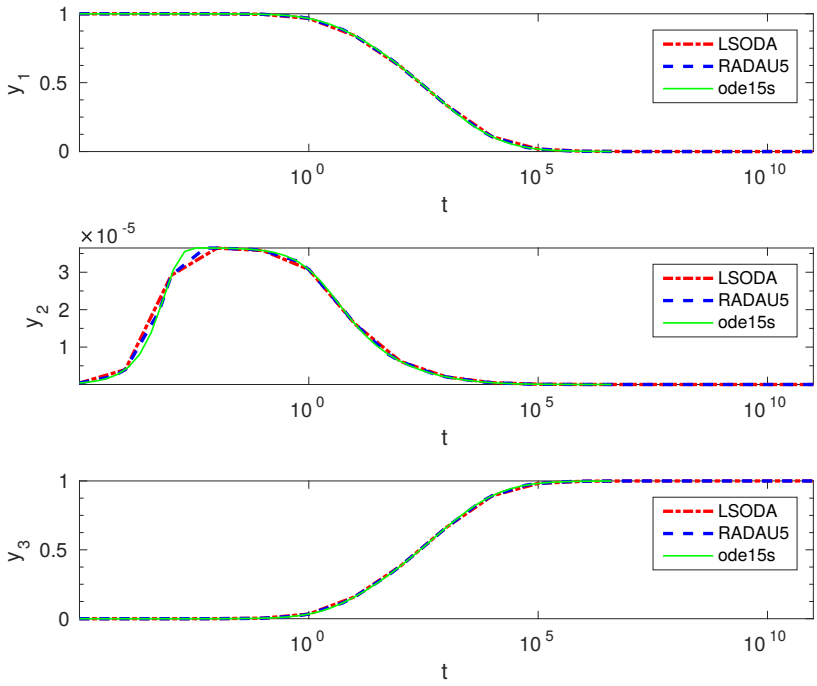

Fig. 26 Computed solution of the Robertson problem by RADAU5, LSODA and ode15s (Matlab) solvers

model with two different constants ($C_s = 0.1$ and $C_s = 0.053$, respectively were applied. For a quantitative validation of the present LES simulations, the averages have been computed by sampling over 50 vortex shedding periods (N_{vs}).

Figure 27 shows the measured and predicted mean stream-wise velocity and its fluctuation as well as the normalised turbulence kinetic energy along the central-line behind the obstacle. In general, all three LES runs matched the experimental data by Sjunnesson et al. [59] reasonably well. The discrepancies between all SGS models were negligible. This finding was supported by the fact that all three runs revealed comparatively the same flow patterns shown in Fig. 28. The differences between the LES and the SASI3 results were small as well. The recirculation zone length was predicted as $< L_r > /H = 1.28$ for all LES runs (and the same as for SASI3), which was in a fairly good agreement with experimental data of Sjunnesson et al. [59], $< L_r > /H = 1.35$.

Figure 29 compares one-dimensional frequency spectra extracted from the present solutions at the downstream location $x/H = 1.75$ on the centerline of the wake. About 6×10^5 samples of the cross-flow velocities were collected (or $N_{vp} \approx 50$). For sake of completeness, the spectrum obtained by SASI3 was added to assess the dissipative properties of the SAS and LES results. It can be seen clearly that the spectra obtained by LES collapsed well and had the similar distribution, meanwhile the SAS spectrum became more dissipative

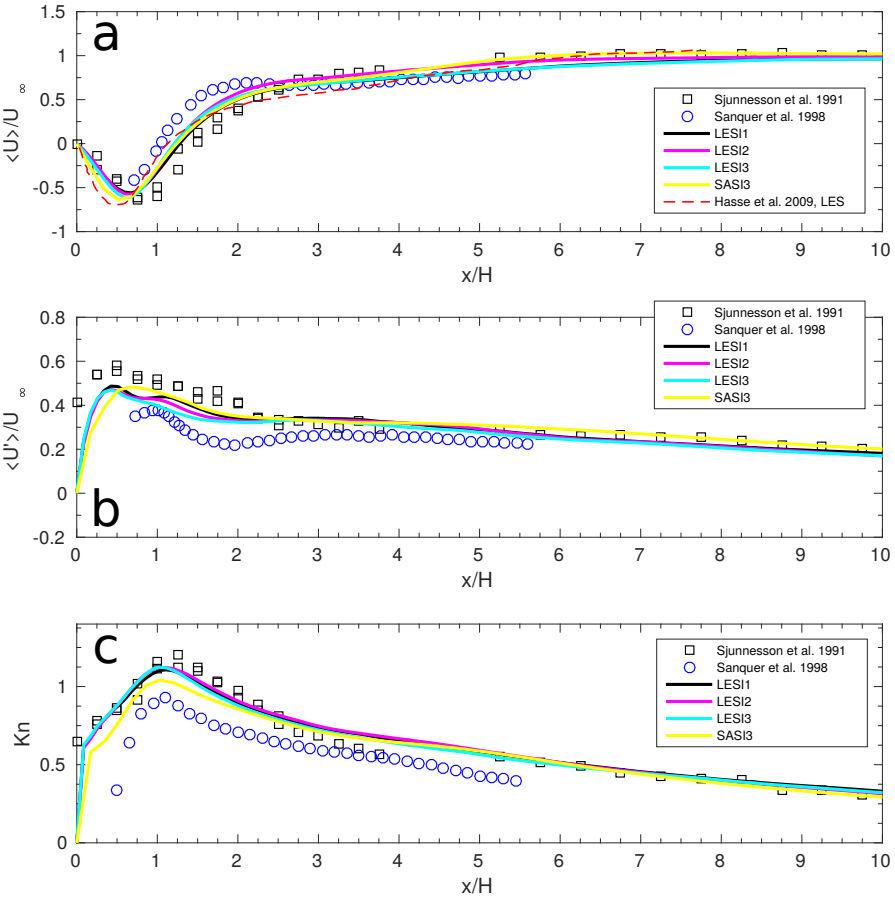

Fig. 27 Normalized mean stream-wise velocity (a), its fluctuations (b) and and normalized turbulence kinetic energy (c) in the wake centerline for the Volvo test rig

after $f/f_{vs} = 2.5$. The Strouhal numbers were St = 0.27, 0.29 and 0.28 for the LESI1, LESI2 and LESI3 runs, respectively. These values were in reasonable agreement with the experimental data by Sjunnesson et al. [59] and Sanquer et al. [54], who measured St = 0.25 and St = 0.26, and corresponded well with the SAS runs.

C Effects of the sub-grid scalar flux modeling for the Volvo test rig

Here, additional inert and reactive LES cases are considered in conjunction with the SGSF closure based on the classical gradient hypothesis closure and Clark's tensor diffusivity model.

The LESI1 case was chosen as baseline to investigate the influence of the SGSF modeling. As the first step, the inert LES run (LESI1a) was calculated

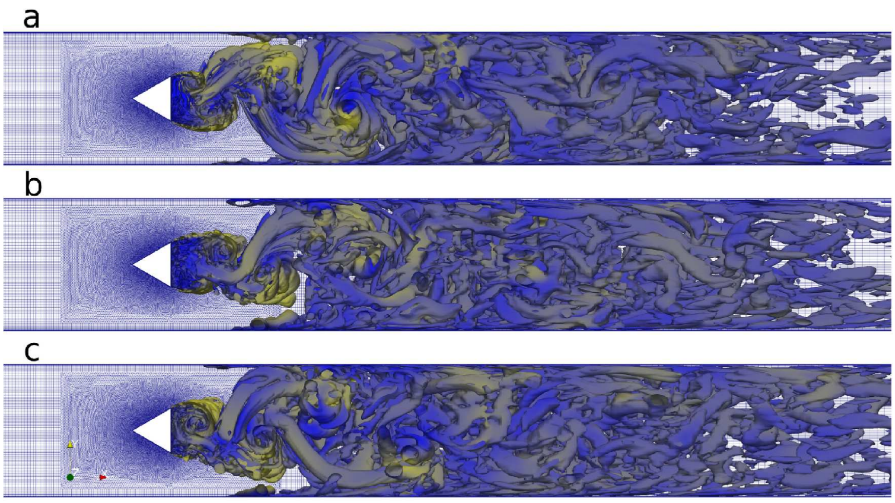

Fig. 28 Flow structures for the Volvo test rig. Iso-surface of the Q-criterion, $Q = 1 \times 10^5$

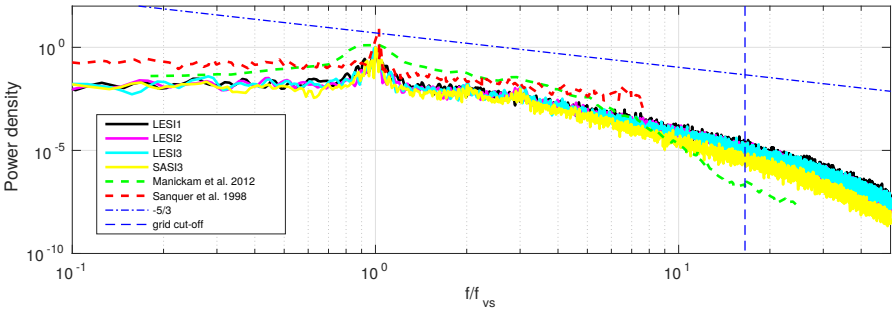

Fig. 29 One-dimensional spectra of the transverse velocity in the wake for the Volvo test rig: non reactive LES results

where the diffusion term in Eq. 14 was replaced in the spirit of Clark's model [10] as

$$F_d = \frac{\Delta^2}{12}\frac{\partial}{\partial x_j}\left(\frac{\partial \tilde{u_j}}{\partial x_j}\frac{\partial \tilde{k}}{\partial x_j}\right). \tag{54}$$

As the second step, the sub-grid scalar flux was replaced in the energy transport equation as

$$\mathbf{b}_h = \frac{\Delta^2}{12}\left(\frac{\partial \tilde{u_j}}{\partial x_j}\frac{\partial \tilde{h}}{\partial x_j}\right), \tag{55}$$

and the inert LES run was performed including both modifications (LESI1b).

Figure 30 compares three cases. Both LESI1a and LESI1b were calculated using identical setup as LESI1. It is clearly seen that differences between all

cases were minor, and no clear advantage could be seen when using the particular SGSF model.

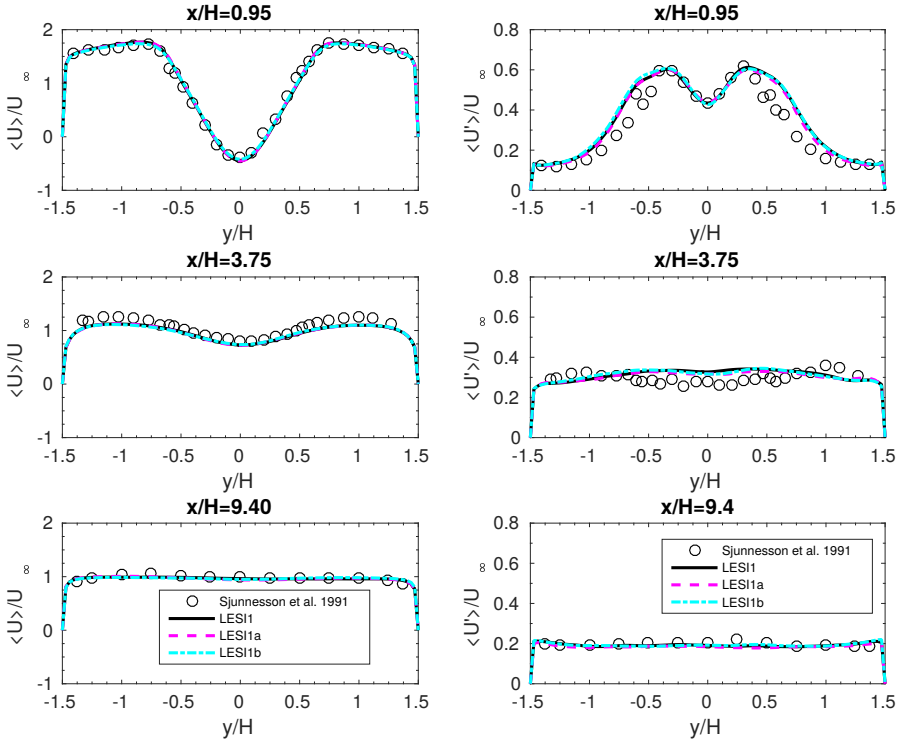

Fig. 30 Normalized mean stream-wise velocity and its fluctuations obtained by LESI1, LESI1a and LESI1b runs in the wake of the Volvo test rig

As the third step, the sub-grid scalar flux was replaced in the species transport equation as

$$\mathbf{b}_s = \frac{\Delta^2}{12}\left(\frac{\partial \tilde{u_j}}{\partial x_j}\frac{\partial \tilde{Y_s}}{\partial x_j}\right). \tag{56}$$

The LESR1 case was chosen to replicate simulations using both Eqs. 55-56 (LESR1a). Figure 31 displays comparison of the normalized, mean temperature and its fluctuations at three axial stages $x/H = 0.95$, 3.75 and 9.4. In general, the discrepancies between two cases are small. The most pronounced difference was observed at $x/H = 0.95$, where the LESR1a case provided the slightly lower peak temperature without impulses in the shear layer regions. The minor differences related to the temperature fluctuations were pronounced as well, however, had the same qualitative trends as the baseline case. The species mole fraction results in Fig. 31 were marginally affected, similar to the line thickness or less.

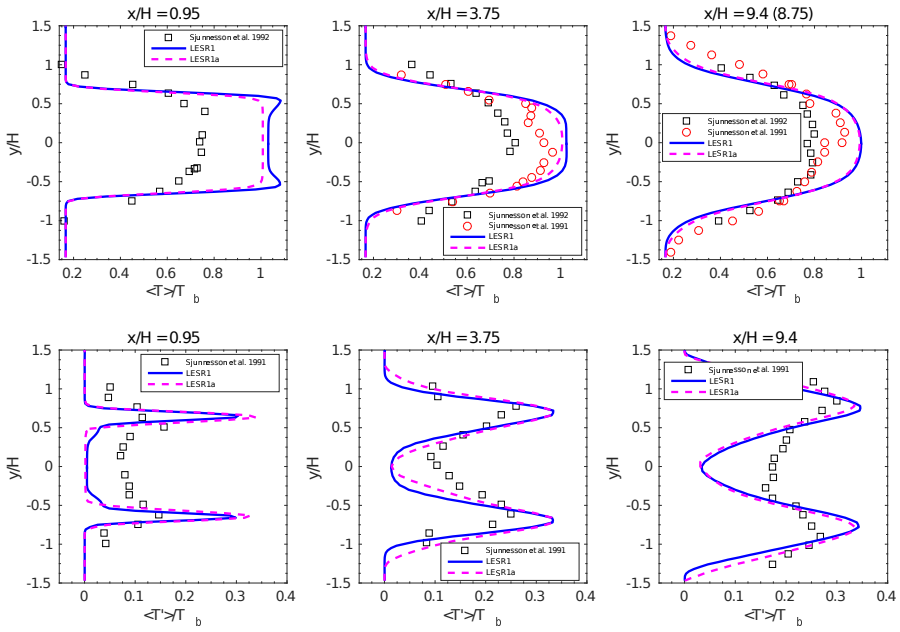

Fig. 31 Normalized mean stream-wise temperature and its fluctuations obtained by LESR1 and LESR1a runs in the wake of the Volvo test rig

References

1. Allauddin, U., Klein, M., Pfitzner, M., Chakraborty, N., A priori and a posteriori analyses of algebraic flame surface density modeling in the context of Large Eddy Simulation of turbulent premixed combustion, Numer. Heat Transfer, Part A: Applications, 71:2, 153-171 (2017)
2. ANSYS FLUENT R13. Theory guide. Tech. rep., Ansys Inc. (2013)
3. Barlow, R. S. and Frank, J. H., Effects of turbulence on species mass fractions in methane/air jet flames, Proc. Combust. Inst. 27, 1087–1095 (1998)
4. Barlow, R. S., Fiechtner, G. J., Carter, C. D., and Chen, J.-Y., Experiments on the scalar structure of turbulent CO/H2/N2 jet flames, Combust. Flame, 120, 549-569 (2000)
5. Baudoin, E., Bai, R. Yu, Nogenmyr, K.J., Bai, X.S., Fureby, C., Comparison of LES models applied to a bluff body stabilized flame, AIAA 2009-1178 (2009)
6. Bowman, C.T., Hanson, R.K., Davidson, D.F., Gardiner, W.C., Lissianski, V., Smith, G.P., Golden, D.M., Frenklach, M., Goldenberg, M.: GRI-Mech (2008). http://www.me.berkeley.edu/gri-mech/. Accessed February 2013
7. Butz, D., Gao, Y., Kempf, A.M., Chakraborty, N., Large eddy simulation of a turbulent premixed swirl flame using an algebraic scalar dissipation rate closure, Combust. Flame, 162, 3180-3196 (2015)
8. Cao, Y., Tamura, T., Large-eddy simulations of flow past a square cylinder using structured and unstructured grids, Comput. Fluids 137, 36–54 (2016)
9. Cheng, P., Dynamics of a radiating gas with application to flow over a wavy wall, AIAA J., 4(2), 238-245 (1966)
10. Clark, R.A., Ferziger, J.H., Reynolds, W.C., Evaluation of subgrid-scale models using an accurately simulated turbulent flow, J. Fluid Mech., 91, 1-16, (1979)
11. Colin, O., Ducros, F., Veynante, D., Poinsot, T., A thickened flame model for large eddy simulations of turbulent premixed combustion, Phys. Fluids., 12, 1843–1863 (2000)

12. Dally, B.B., Masri, A.R., Barlow, R.S. and Fiechtner, G.J., Instantaneous and mean compositional structure of bluff-body stabilised nonpremixed flames. Combust. Flame, 114, 119–148 (1998)
13. Dunkle, R.V., Geometric mean beam lengths for radiant heat transfer calculations, ASME J. Heat Transfer, 86(1), 75-80 (1964)
14. Dunn, M. J., Masri, A. R. and Bilger, R. W., A new piloted premixed jet burner to study strong finite-rate chemistry effects, Combust. Flame 151(1-2), 46–60 (2007)
15. Dunn, M. J., Masri, A. R., Bilger, R. W., Barlow, R. S. and Wang, G. H., The compositional structure of highly turbulent piloted premixed flames issuing into a hot coflow, Proc. Combust. Inst. 32(2), 1779–1786 (2009)
16. Ertesvåg, I. S. and Magnussen, B. F., The eddy dissipation turbulence energy cascade model, Combust. Sci. Technol. 159, 213–235 (2000)
17. Geurts, B., Elements of direct and large-eddy simulation, R.T.Edwards, Philadelphia (2004)
18. Gobbert, M.K., Robertson's example for stiff differential equations, Technical report, Arizona State University (1996)
19. Gran, I. R. and Magnussen, B. F., A numerical study of a bluff-body stabilized diffusion flame. Part 2. Influence of combustion modeling and finite-rate chemistry, Combust. Sci. Technol. 119, 191-217. (1996)
20. Hairer, E. and Wanner, G., Solving Ordinary Differential Equations II: Stiff and Differential-Algebraic Problems, Springer Series in Computational Mathematics, 2nd rev. ed, Springer-Verlag (1996)
21. Harten, A., High resolution schemes for hyperbolic conservation laws, J. Comput. Phys., 49, 357-393 (1983)
22. Hasse, C., Sohm, V., Wetzel, M., Durst, B. Hybrid URANS/LES turbulence simulation of vortex shedding behind a triangular flameholder, Flow Turbul. Combust. 83, 1-20 (2009)
23. Issa, R., Solution of the implicitly discretized fluid flow equations by operator splitting, J. Comput. Phys., 62, 40–65 (1986)
24. Jasak, H., Weller, H.G., Gosman A.D., High resolution NVD differencing scheme for arbitrarily unstructured meshes, Int. J. Numer. Meth. Fluids, 31, 431–449 (1999)
25. Jones, W.P., Whitelaw, J.H., Calculation methods for reacting turbulent flows: a review, Combust. Flame, 48, 1-26 (1982)
26. Jones, W.P., Marquis, A.J., Wang, F., Large eddy simulation of a premixed propane turbulent bluff body flame using the Eulerian stochastic field method, Fuel, 140, 514-525 (2015)
27. Karpov, V.P., Lipatnikov A.N., Zimont, V.L., A test of an engineering model of premixed turbulent combustion, Proc. Combust. Inst., 26, 249-257 (1996)
28. Klein, M., Chakraborty, N., Pfitzner, M., Analysis of the combined modelling of subgrid transport and filtered flame propagation for premixed turbulent combustion, Flow Turbul. Combust., 96, 921-938 (2016)
29. Launder, B., Spalding, D., The numerical computation of turbulent flows, Comput. Methods Appl. Mech. Eng., 3(2), 269–289 (1974)
30. Lilleberg, B., Christ D., Ertesvåg, I.S., Rian, K.E., Kneer, R., Numerical simulation with an extinction database for use with the Eddy Dissipation Concept for turbulent combustion, Flow Turbul. Combust., 91, 319-346 (2013)
31. Lysenko, D.A., Ertesvåg, I.S., Rian, K.E., Modeling of turbulent separated flows using OpenFOAM, Comput. Fluids, 80, 408-422 (2013)
32. Lysenko, D.A., Ertesvåg, I.S., Rian, K.E., Large-eddy simulation of the flow over a circular cylinder at Reynolds number 3900 using the OpenFOAM toolbox, Flow Turbul. Combust., 89, 491–518 (2012)
33. Lysenko, D.A., Ertesvåg, I.S., Rian, K.E., Large-eddy simulation of the flow over a circular cylinder at Reynolds number 2×10^4, Flow Turbul. Combust., 92, 673-698 (2014)
34. Lysenko, D.A., Ertesvåg, I.S., Rian, K.E., Numerical simulation of non-premixed turbulent combustion using the Eddy Dissipation Concept and Comparing with the Steady Laminar Flamelet Model, Flow Turbul. Combust., 93, 577–605 (2014)
35. Lysenko, D.A., Ertesvåg, I.S., Rian, K.E., Numerical simulations of the Sandia flame D using the Eddy Dissipation Concept, Flow Turbul. Combust., 93, 665–687 (2014)

36. Ma, T., Gao, Y., Kempf, A.M., Chakraborty, N., Validation and implementation of algebraic LES modelling of scalar dissipation rate for reaction rate closure in turbulent premixed combustion, Combust. Flame, 161, 3134-3153 (2014)
37. Magnussen, B.F., Hjertager, B.H., On mathematical modeling of turbulent combustion with special emphasis on soot formation and combustion, Proc. Combust. Inst., 16, 719–729 (1976)
38. Magnussen, B.F., Modeling of NOx and soot formation by the Eddy Dissipation Concept. Int.Flame Research Foundation, 1st topic Oriented Technical Meeting., 17-19 Oct. 1989. Amsterdam, Holland
39. Magnussen, B.F., The Eddy Dissipation Concept a bridge between science and technology, In: ECCOMAS Thermal Conference on Computational Combustion, Lisbon (2005)
40. Manickam, B., Franke, J., Muppala, S.P.R., Dinkelacker, F., Large-eddy simulation of triangular-stabilized lean premixed turbulent flames: quality and error assessment, Flow Turbul. Combust., 88, 563-596 (2012)
41. Menter, F., Esch, T., Elements of industrial heat transfer prediction, 16th Brazilian Congress of Mechanical Engineering (COBEM) (2001)
42. Menter, F. R., Kuntz, M., Langtry, R., Ten years of industrial experience with the SST turbulence model, Turbulence, Heat and Mass Transfer 4,625-632 (2003)
43. Menter, F.R., Egorov, Y., Formulation of the Scale-Adaptive Simulation (SAS) model during the DESIDER Project, In: Haase, W., Braza, M., Revell, A. (eds.) Notes on Num. Fluid Mech Multidisc Design, 103, Springer (2009)
44. Menter, F.R., Egorov, Y., The Scale-Adaptive Simulation method for unsteady turbulent flow predictions. Part 1: Theory and model description, Flow Turbul. Combust., 85, 113-138 (2010)
45. Nicoud, F.,Ducros, F., Subgrid-scale stress modelling based on the square of the velocity gradient tensor, Flow Turbul. Combust, 62, 183–200 (1999)
46. O'Malley, R.E., Singular Perturbation Methods for Ordinary Differential Equations, Springer-Verlag, New York (1991)
47. Peters, N., Turbulent Combustion, Cambridge University Press (2000)
48. Radhakrishnan, K., Hindmarsh, A.C., Description and use of LSODE, the Livermore solver for ordinary differential equations, Lawrence Livermore national laboratory report, UCRL-ID-113855 (1993)
49. Rhie, C., Chow, W., Numerical study of the turbulent flow past an airfoil with trailing edge separation. AIAA J., 21, 1525–32 (1983)
50. Robertson, H.H., The Solution of a set of reaction rate equations, J. Walsh (Ed.), Numerical Analysis: an Introduction, pp. 178-182., Academic Press, London (1966)
51. Sabelnikov, V., Fureby, C., LES combustion modeling for high Re flames using a multiphase analogy, Combust. Flame, 160, 83–96 (2013)
52. Sagaut, P., Large Eddy Simulation for Incompressible Flows, 3rd ed., Springer Berlin, (2006)
53. http://web.eng.ucsd.edu/mae/groups/combustion/mechanism.html, Update on 2014-10-04.
54. Sanquer,S., Bruel, P., Deshaies, B., Some specific characteristics of turbulence in the reactive wakes of bluff bodies, AIAA J., 36(6) (1998)
55. Sathiah, P., Lipatnikov, A., Effects of flame development on stationary premixed turbulent combustion, Proc. Comb. Inst., 31, 3115–3122 (2007)
56. Shampine, L.F., Reichelt, M. W., The MATLAB ODE Suite, SIAM J. Sci. Comput., 18, 1-22 (1997)
57. Shanbhogue, S.J., Husain, S., Lieuwen, T., Lean blowoff of bluff body stabilized flames: scaling and dynamics, Prog. Energy Combust. Sci., 35, 98-120 (2009)
58. Sjunnesson, A., Olovsson, S., Sjöblom, B., Validation rig – a tool for flame studies, VOLVO Aero AB, S-461 81, Trollhättan, Sweden (1991)
59. Sjunnesson, A., Nelson, C., Max, E., LDA measurements of velocities and turbulence in a bluff body stabilized flame, Laser Anemometry 3, ASME (1991)
60. Sjunnesson, A., Henriksson, P., Löfström, C., CARS measurements and visualization of reacting flows in a bluff body stabilized flame, AIAA 92-3650 (1992)
61. Smagorinsky, J.S., General circulation experiments with primitive equations, Mon. Weather Rev., 91(3), 99–164 (1963)

62. Smith, T.F., Shen, Z.F. and Friedman, J.N. , Evaluation of coefficients for the weighted sum of gray gases model, ASME J. Heat Transfer, 104(4), 602–608 (1982)
63. Vandoormaal, J.P., Raithby, G.D., Enhancements of the SIMPLE method for predicting incompressible fluid flows, Numer. Heat Transfer, 7, 147–163 (1984)
64. Warnatz, J., Maas, U., Dibble R.W., Combustion, 4th ed. Springer. Berlin Heidelberg New York (2006)
65. Waterson, N.P., Deconinck, H., Design principles for bounded higher-order convection schemes – a unified approach, J. Comput. Phys., 224, 182–207 (2007)
66. Welch, P., The use of fast Fourier transform for the estimation of power spectra: a method based on time averaging over short, modified periodograms. IEEE Trans. Audio Electroacoust. 15(6), 70-73 (1967)
67. Weller, H.G., Tabor, G., Jasak H., Fureby, C., A tensorial approach to computational continuum mechanics using object-oriented techniques, Comp. Phys., 12(6), 620–631 (1998)
68. Westbrook, C. K., Dryer, F. L., Simplified reaction mechanisms for the oxidation of hydrocarbon fuels in flames, Combust. Sci. Technol. 27, 31–43 (1981)
69. Westbrook, C. K., Dryer, F. L., Chemical kinetic modeling of hydrocarbon combustion, Prog. Energy Combust. Sci. 10, 1–57 (1984)
70. Yasari, E., Verma, S., Lipatnikov, A.N., RANS simulations of statistically stationary premixed turbulent combustion using flame speed closure model, Flow Turbul. Combust., 94, 381–414 (2015)
71. Yoshizawa, A., Statistical theory for compressible shear flows, with the application to subgrid modelling, Phys. Fluids 29(2152), 1416-1429 (1986)
72. Zimont, V.L., Lipatnikov, A.N., A numerical model of premixed turbulent combustion of gases, Chem. Phys. Rep., 14, 993-1025 (1995)